Developing and Characterizing Sources of Quantum States of Light: from Single Photons to Million-Photon Fock States

by

Sahil Pontula

Submitted to the Department of Physics
in partial fulfillment of the requirements for the degree of

Bachelor of Science in Physics

at the

MASSACHUSETTS INSTITUTE OF TECHNOLOGY

May 2023

Author .....
Department of Physics
May 12, 2023

Certified by .....
Marin Soljačić
Professor of Physics
Thesis Supervisor

Accepted by .....
Lindley Winslow
Associate Head, Department of Physics

Developing and Characterizing Sources of Quantum States of Light: from Single Photons to Million-Photon Fock States

by

Sahil Pontula

Submitted to the Department of Physics
on May 12, 2023, in partial fulfillment of the
requirements for the degree of
Bachelor of Science in Physics

Abstract

One of the central goals of quantum optics is the generation and control of quantum states of light. Chief among these states are Fock states, the fundamental eigenstates of the electromagnetic Hamiltonian with a perfectly-defined photon number. Decades of research have been devoted to producing Fock states, but no known source can produce Fock states at macroscopic intensities and optical wavelengths. Such a source would revolutionize applications ranging from all-optical quantum information processors to quantum sensing far below the shot noise limit. Here, I describe two projects related to the development of quantum states of light, focusing on Fock state sources. First, I demonstrate an improved characterization of single photon emitters (SPEs) in hexagonal boron nitride (hBN) at optical wavelengths. Specifically, I demonstrate how one can extract information about electron-phonon coupling in SPEs from photoluminescence spectra in order to characterize fidelity in generating $N = 1$ Fock states. Second, I consider methods for generating $N \gg 1$ Fock states. I describe a novel method to generate highly intensity-noise squeezed states of light and demonstrate the feasibility of their production on existing semiconductor lasers. This method combines nanophotonics and nonlinear optics to generate photonic dissipation ("nonlinear dispersive loss") that depends nonperturbatively on the photon number itself. This allows unprecedented squeezing of the intracavity photon number distribution, approaching Fock states of millions of photons. I provide a thorough analysis of intensity and phase noise in these semiconductor lasers and propose realistic platforms amenable to the effects described here.

Thesis Supervisor: Marin Soljačić
Title: Professor of Physics

Acknowledgments

I acknowledge my current faculty advisor, Marin Soljačić, and my supervisors, Jamison Sloan and Nick Rivera, for their guidance along my journey exploring nonlinear and quantum optics. I would also like to thank my other research supervisors, Phiala Shanahan and Dan Hackett, for their advice as I navigated my interests in physics. Going further back, I thank my former research mentors, Peter Lu and Abhichart Krissanaprasit, with whom I worked starting in high school, as well as Hamidreza Akbari, Pankaj Jha, and Harry Atwater, with whom I worked during Summer 2021 at Caltech. Their incredible guidance kept my spark of curiosity and innovation going. This work would also not be possible without the financial support of the Undergraduate Research Opportunities Program as well as the National Science Foundation and Hertz Fellowship Foundation, which will fund me as a graduate student. Lastly, I thank my family for their unfailing support through everything.

Contents

List of Figures

3-4 **Effects of carrier and Kerr nonlinearities composed with dispersive loss**. (a) Schematically, in the presence of only carrier nonlinearity σ, the resonance frequency and thus loss depend "directly" on carrier density N. Thus, "gain equals loss" implies $G(N) = \kappa(N)$ (both plotted as a function of the ratio of mean carrier density to transparency density). For sufficiently strong σ and low background loss κ_0, multiple steady state carrier densities N can correspond to a given photon number n, resulting in different losses (detunings from the Fano resonance). The lowest loss solution (smallest detuning) is most likely to lase, though extra solutions may be accessible by dynamic pumping schemes. (b) The schematic effect of this "carrier bistability" is to create multiple branches in the S-curve of different slope/threshold current. Interesting features emerge when both carrier and Kerr nonlinearities are present, resulting in the behaviors shown in panels (c), (d), and (e). In particular, the carrier nonlinearity causes a deformation of the intensity-nonlinear Lorentzian loss profile, eventually pinching off the "sharp loss" from the linear loss for sufficiently strong carrier nonlinearity (purple curve). This stems from leftward motion of the carrier bistability boundaries and creates a demarcation between linear ($F \gg 1$) and nonlinear ($F < 1$) loss regimes which may be separated by a region of lasing with no stable solution. System parameters used are the same as those in Fig. 3-3 with a nonlinear strength $\beta = -10^{-10}$, background loss $\kappa_0 = 10^{-2} \cdot \mathrm{FSR}$, and Fano resonance decay $\gamma = 2 \times 10^{12}$ rad/s. The magnitudes of Kerr and carrier nonlinearities taken here are comparable to what they might be in GaAs-based gain media: $\beta \sim -10^{-10}$ and $\sigma \sim -3 \times 10^{-27}$ m^3 (with the proviso of being taken as instantaneous and being evaluated at a single wavelength). Note also that the Kerr nonlinearity varies with mode volume (here, I consider a mode volume equal to the cavity volume). 59

List of Tables

Chapter 1

Introduction

One of the main goals of quantum optics as a field is to generate and control quantum states of light. This is an intriguing objective both from a fundamental physics point of view as well as from an applied perspective. Quantum states of light do not naturally occur and are often destroyed with the slightest presence of noise or loss, but their potential in everything from optical quantum computers to enhanced biosensors is tantalizing [4]. I provide three examples of quantum light and the potential applications they may unlock:

1. **Squeezed states.** In the family of squeezed states, the uncertainty in one observable reduces at the expense of the other, while still maintaining Heisenberg's uncertainty principle. A practical example of such a pair of variables is that of photon number (amplitude) and phase. States of light squeezed in photon number promise numerous applications in quantum information and sensing, allowing, for example, signal detection below the shot noise limit [4]. In the limit of infinite number squeezing, one approaches a so-called Fock state, an energy eigenstate of the electromagnetic field Hamiltonian with perfectly defined photon number n. This state can be used to realize numerous quantum computing protocols that require operations on photon number, such as boson sampling [5]. In the area of sensing, phase-squeezed vacuum has already been employed by LIGO to improve phase sensitivity to gravitational waves

[6]. Photon number-squeezed quantum sources of light could enable below-shot noise sensing and metrology.

2. **Superposition and entangled states.** The notion of superposition states is a well-known manifestation of quantum mechanics often exemplified by the famous Schrodinger cat thought experiment. Superposition and entangled states of light, such as a superposition of Fock states, is immensely valuable to realizing logic gates at the single-photon level in all-optical quantum computers. A reliable source of such states would revolutionize quantum optical information processing and pave the way towards significant advances over classical computers [7]. Relatedly, numerous protocols in quantum cryptography rely on entangled photon states for secure encryption and decoding of quantum information, unachievable by classical methods [8].

3. **Entangled photon-matter hybrid quantum states.** Strongly coupled photonic quasiparticles, such as polaritons, are entangled light-matter states that possess both photonic and matter-like character [9]. The strong coupling regime of light-matter interactions has enabled incredible applications, from ultralow threshold polaritonic lasers to modified chemical kinetics to quantum batteries employing superabsorption. Polaritons emerging from ultrastrong coupling (USC) between light and matter may enable the unprecedented ability to engineer material properties, including superconductivity and optical nonlinearity. USC has garnered significant recent theoretical and experimental interest and is actively being explored through multiple lenses, from quantum chemistry to quantum optics.

Despite these promising applications, the reliable production of many quantum states of light remains quite difficult and is an area of active research. In this thesis, I describe my undergraduate research in developing and characterizing sources of quantum light, focusing on the generation of Fock states and highly intensity noise-squeezed states.

Chapter 2 describes my work at Caltech in characterizing single photon emission in hexagonal boron nitride, a 2D van der Waals material. I demonstrate how hBN can host extraordinarily efficient color centers (defects) that emit single photons ($N = 1$ Fock states) and discuss practical limitations on this efficiency due to electron-phonon coupling.

Chapter 3 describes my work at MIT in developing the theoretical foundations and proposing experimental platforms for a laser capable of generating highly intensity noise-squeezed states of light approaching Fock states with millions of photons. This could pave the way to the first "Fock laser," a source of optical/near-IR Fock states at macroscopic intensities.

Finally, in Chapter 4, I conclude and discuss a few exciting avenues that my work has opened in the direction of quantum light generation

Chapter 2

Isotopic Hexagonal Boron Nitride Single Photon Emitters

2.1 Introduction

Single-photon quantum emitters have emerged as promising candidates for application in quantum information, photonics, and sensing, among other fields, exhibiting important quantum effects such as photon antibunching [10, 11]. To this end, solid-state network covalent materials such as diamond, silicon carbide, gallium nitride, zinc oxide, and boron nitride (BN) have been engineered with atomic defects known as "color centers" that act as single-photon emitters [12, 13, 14, 15]. However, to be viable for on-chip integration into photonic devices, 2D layered van der Waals materials are preferred. Furthermore, it is important that the material shows high brightness at room temperature. For these reasons, hexagonal boron nitride (hBN) has recently garnered much interest as a bright single-photon quantum emitter in the visible range at room temperature [16].

Ideally, single-photon emitters should exhibit minimal coupling to phonons (quantum lattice vibrational modes) within a material, so that phenomena such as line broadening (acoustic phonons) and the presence of phonon side bands (optical phonons) are suppressed [17]. In this case, in the absence of line broadening effects due to spectral diffusion and phonon coupling, the emitter is only Fourier transform limited

by the uncertainty principle, making it suitable for multiple quantum applications. Future work involves engineering hBN quantum emitters as building blocks for a quasi-noiseless optical amplifier, whereby single-photon stimulated emission is capable of amplifying very weak optical signals by adding photons coherently and thus increasing the signal to noise ratio [18]. Prior work has used conductive substrates to reduce the noise introduced by spectral diffusion, but the temperature-dependent effect of phonon noise (which is negligible at cryogenic temperatures but dominates at room temperature) remains and has been difficult to address [19]. The main reason for this is that different emitters within the same crystal can have different phonon side band profiles, so that phononic effects can vary considerably between samples.

The importance in identifying electron-phonon coupling in hBN emitters is twofold. Through the Huang-Rhys factor, one can probe correlations with ZPL broadening and PSB profiles. Through the PDOS, information about coupling to both lattice and local phonon modes can be extracted. Two key measures for doing so are the Debye-Waller and Huang-Rhys factors. The former is well-characterized for hBN and reflects the relatively high amount of spectral energy density that lies in the zero-phonon line compared to phonon side bands. The latter more accurately describes emitter-phonon coupling strength by measuring the displacement between ground and excited electronic states due to the coupling. Figure 2-1 provides an overview of the detection of single-photon emission and the manifestation of electron-phonon coupling.

2.2 Methodology

2.2.1 Theoretical fit

Photon-mediated transitions in a material like hBN are complicated by electron-phonon coupling, which results in so-called phonon side bands (PSB) in the photoluminescence (PL) spectrum of the material, shifted redward relative to the zero-phonon line (ZPL) that does not feature an exchange of phonons. To quantify the strength of the ZPL, I used a fitting procedure involving the Huang-Rhys factor S_{HR}, which

quantifies the average number of phonons emitted in a transition ($S_{\mathrm{HR}} \approx 0$ if the zero-phonon line dominates the PL spectrum). The theory and application of this procedure to defects in diamond have been reported previously [20, 21, 22]. The free parameters in the fit are the central energy and FWHM of the ZPL, which is modeled by the corresponding Lorentzian $I_0(E)$, S_{HR}, and the one-phonon spectral distribution $I_1(E)$ which gives the probability that a phonon of energy E is emitted, increasing the energy of the lattice surrounding the defect (the function is also defined for $E < 0$, corresponding to phonon absorption). The fitting function is summarized by

$$L(E) = e^{-S_{\mathrm{HR}}} I_0(E) + I_0(E) \otimes \left(\sum_n e^{-S_{\mathrm{HR}}} \frac{S_{\mathrm{HR}}^n}{n!} I_n(E) \right), \tag{2.1}$$

where

$$I_n(E) = I_1(E) \otimes I_{n-1}(E). \tag{2.2}$$

Here, $L(E)$ is directly determinable experimentally from the PL spectrum via

$$L(E) = S(E)/E^3. \tag{2.3}$$

The division by E^3 is necessary to normalize out the effect of spontaneous emission. This procedure has shown excellent fits even for spectra with broad ZPLs and multiple phonon side bands. It also enables us to extract S_{HR}, to quantify the efficiency of hBN emitters, as well as the phonon density of states $g(E)$, which is directly related to $I_1(E)$ via

$$I_1(E) \propto (n(E) + 1) \frac{\hbar^3 g(E)}{E^2}. \tag{2.4}$$

The phonon density of states is difficult to obtain directly by experiment, so this method provides an excellent way to learn about both local and global vibrational modes that couple strongest to defect-site electrons.

Fitting parameters

In addition to the Huang-Rhys factor S_{HR}, modeling the ZPL as a (normalized) Lorentzian introduces two additional degrees of freedom. The last fitting parameter is the function $g(E)$, or equivalently $I_1(E)$. I explore two approaches to parametrizing this function:

1. discretizing $g(E)$ with some step size $dE \approx 5$ meV and up to some maximum energy $E_{\mathrm{max}} \approx 200$ meV (beyond which there are no more theoretically predicted peaks in the PDOS for hBN), treating all discrete points as fitting parameters and

2. treating $I_1(E)$ as a sum of n Lorentzians, where $n \leq 5$ is typically chosen.

The latter greatly reduces the number of fitting parameters (and thus also the likelihood of overfitting) while still maintaining a low reduced chi-squared value. Both methods allow extraction of S_{HR} and the ZPL parameters to a fairly high accuracy, but (2) may allow more accurate estimation of the energies of phonon modes to which electrons couple most strongly since it is not restricted by discretization. It is also possible to model $g(E)$ as a sum of Lorentzians instead (roughly corresponding to peaks in the PDOS), but I find that the fitting is considerably slower and not as good, converging on local optima.

The inclusion of E_{max} in the discretized-based fit is also somewhat restrictive ($g(E)$ is padded outside of the range $[0, E_{\mathrm{max}}]$). If I were to neglect it and use the maximum phonon energy defined by the dataset, a coarser resolution dE would be necessary to prevent overfitting. This is not a problem for the Lorentzian-based fit. I do sometimes see peaks in the predicted PDOS from this method above 220 meV, but these are attributed to emission of multiple phonons whose energies are seen as lower-energy peaks in the PDOS. These higher-energy peaks are trimmed when reporting the one-phonon PDOS in the range $[0, E_{\mathrm{max}}]$.

Constraints sometimes need to be imposed to obtain physically reasonable fits. In particular, for spectra with lower Debye-Waller factors and more prominent PSBs, it is necessary to have $\frac{g(E)}{E^2} \to 0$ as $E \to 0$ to enforce consistency with deformation

potential coupling at low phonon energies. Without this constraint, the goodness of fit is not compromised, but bunching of I_n for $n > 0$ near the ZPL is observed, yielding an artificially high S_{HR}. To enable faster fitting, I also sometimes fix two modes to be fit around 165 and 195 meV, corresponding to well-known longitudinal optical (LO) modes.

2.2.2 Experimental protocol

Isotopic hBN crystals are exfoliated onto a PDMS silicone substrate and subsequently transferred to a silicon/silicon dioxide chip at 80°C. Defects are introduced in the crystal by annealing in a vacuum chamber at temperature 850°C and pressure 1.2 torr, with argon gas flow rate 300 mL/min. Microscopy is used to characterize the crystal at each stage of this process.

The crystals are then characterized optically using confocal microscopy and photoluminescence (PL) spectroscopy. The latter involves excitation with a 532 nm laser. Scans across regions of the sample are performed using a fast scanning mirror (FSM). Once regions with candidate single-photon sources are discerned from the PL maps, atomic force microscopy (AFM) is used to perform thickness measurements of the crystal in these regions and the single-photon source PL spectrum is collected. Follow-up g_2 correlation measurements can be used to confirm the single-photon sources. The collected functions $g_2(\tau)$ are expected to show a dip at $\tau = 0$, characteristic of the antibunching property of single-photon emission.

2.3 Results

Before performing experiments, sample exfoliated hBN datasets were fitted using the Huang-Rhys procedure. Figure 2-2 shows fits and extracted PDOS for the same sample at two different temperatures. Thermal broadening of the ZPL due to quadratic electron-phonon coupling is observed. I also see that overall agreement in the position of peaks in the PDOS is seen for the Lorentzian-based and discretized-based methods, with some discrepancies attributed to overfitting in the latter method.

2.3.1 Isotopic hBN optical characterization

Optical characterization of nine $hB^{10}N$ and three $hB^{11}N$ SPEs was performed. Confocal microscope images and integrated PL maps of two sample crystals are shown in Figure 2-3. The fitted PL spectra and extracted PDOS for two emitters are shown in Figure 2-4. A fit involving Lorentzian-based $I_1(E)$ was not performed for the $hB^{11}N$ emitter because of the prediction of an unphysically broad peak around 200 meV. This can still be seen for the discretized-based fit in Figure 2-4d. Further constraints on the fit will be implemented to remove this artifact.

2.3.2 Phonon density of states

The phonon density of states (PDOS) for isotopic hBN has previously been determined using density functional theory (DFT), as shown in Figure 2-5a [3]. Peaks in the PDOS correspond to global in-plane and out-of plane optical and acoustic phonon modes throughout the lattice. The peaks at ≈ 165 meV and ≈ 195 meV are in-plane longitudinal optical (LO) modes for which I observe strong coupling for most emitters (including those shown above). Figure 2-5b shows the experimentally-predicted PDOS for $hB^{10}N$ and $hB^{11}N$ obtained by averaging over all available emitters using the discretized-based fit. An analogous plot will be obtained for the Lorentzian-based fitting method.

Given the resolution of the discretized function $g(E)$ was 5 meV, approximately the largest observable shift in corresponding phonon modes between the two isotopic varieties of hBN in Figure 2-5a, and the small sample size thus far, I cannot discern the expected shift in phonon modes (particularly LO modes around ≈ 165 meV and ≈ 195 meV). Local strain and other effects can induce variations about these two energies, giving another reason for why a larger sampling size is necessary before taking an appropriate statistical average.

2.4 Outlook

I have demonstrated the application of the Huang-Rhys fitting method to isotopic hBN single-photon emitters, obtaining excellent fits to experimental PL spectra and extracting useful parameters governing electron-phonon coupling, including ZPL FWHM, Huang-Rhys factor, and predicted PDOS. The extracted PDOS demonstrates strong coupling to lattice LO phonon modes at $\approx$ 165 meV and $\approx$ 195 meV, as expected from previous work [14].

I hope to vastly increase the sample size for isotopic hBN SPEs, as this will allow more accurate extraction of the energies of phonon modes (both local and global) that induce strongest coupling. Furthermore, I would like to test the hypothesis of theoretically-predicted shifts in the aforementioned LO modes between the two isotopes. The largest shift occurs for high-energy LO modes and requires a resolution of $\leq$ 5 meV [3]. Other predictions I hope to test include ZPL broadening of naturally-occurring hBN due to its mass impurity, broadening due to stronger coupling to acoustic phonons, and shifts in the energies of phonon modes due to variations in crystal thickness. I envision that larger sample sizes will also allow extraction of correlations between ZPL FWHM, Huang-Rhys factor, and PDOS amplitudes indicative of strength of electron-phonon coupling.

Future experimental steps include collection of PL spectra for isotopic samples at varying temperatures, to examine temperature dependence of the Huang-Rhys factor and PDOS, as well as collection of PLE spectra. The latter provides another way to estimate the Huang-Rhys factor via the Stokes shift and could provide finer resolution of the PDOS.

Overall, this method has provided a convenient way to probe electron-phonon coupling and phonon density of states via a tabletop optical experiment, without the use of complicated experimental methods such as neutron scattering. In the long term, I hope to use this method to probe conclusive signatures of the structure of the color center and even engineer better emitters by suppressing coupling to the strongest phonon modes.

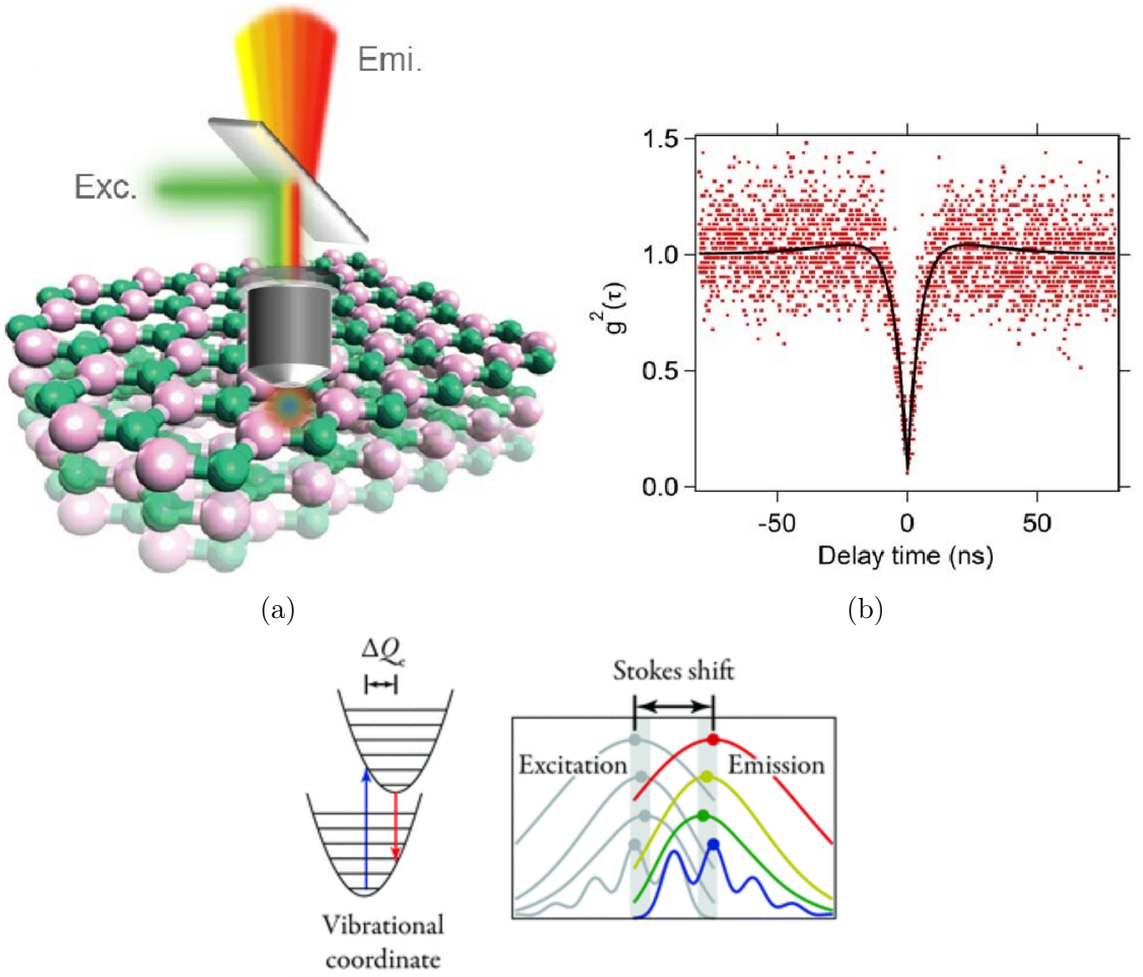

Figure 2-1: (a): Excitation of the color center by a 532 nm laser and resulting photoluminescence at 600 nm [1]. (b): Typical antibunching dip in $g_2(\tau)$ correlation function at $\tau = 0$, indicative of single-photon emission [1]. (c): Non-radiative transitions accompanying photoluminescence process. These correspond to lattice relaxation and result in phonon emission, which is quantified by the Huang-Rhys factor and the related Stokes shift [2].

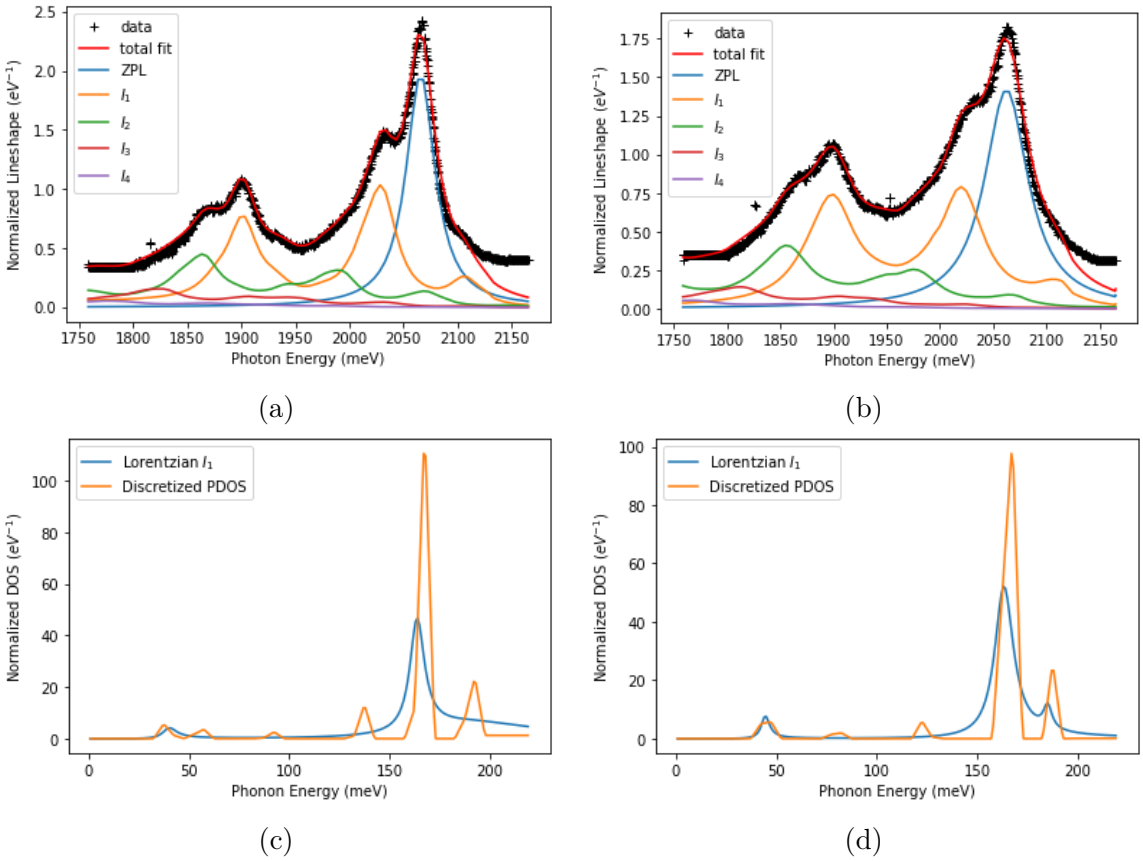

Figure 2-2: Fits to sample exfoliated hBN PL spectra collected at (a) 30°C (left) and (b) 100°C (right). Their corresponding predicted PDOS (using both discretized $g(E)$ and Lorentzian-based $I_1(E)$) are shown in figures (c) and (d) respectively.

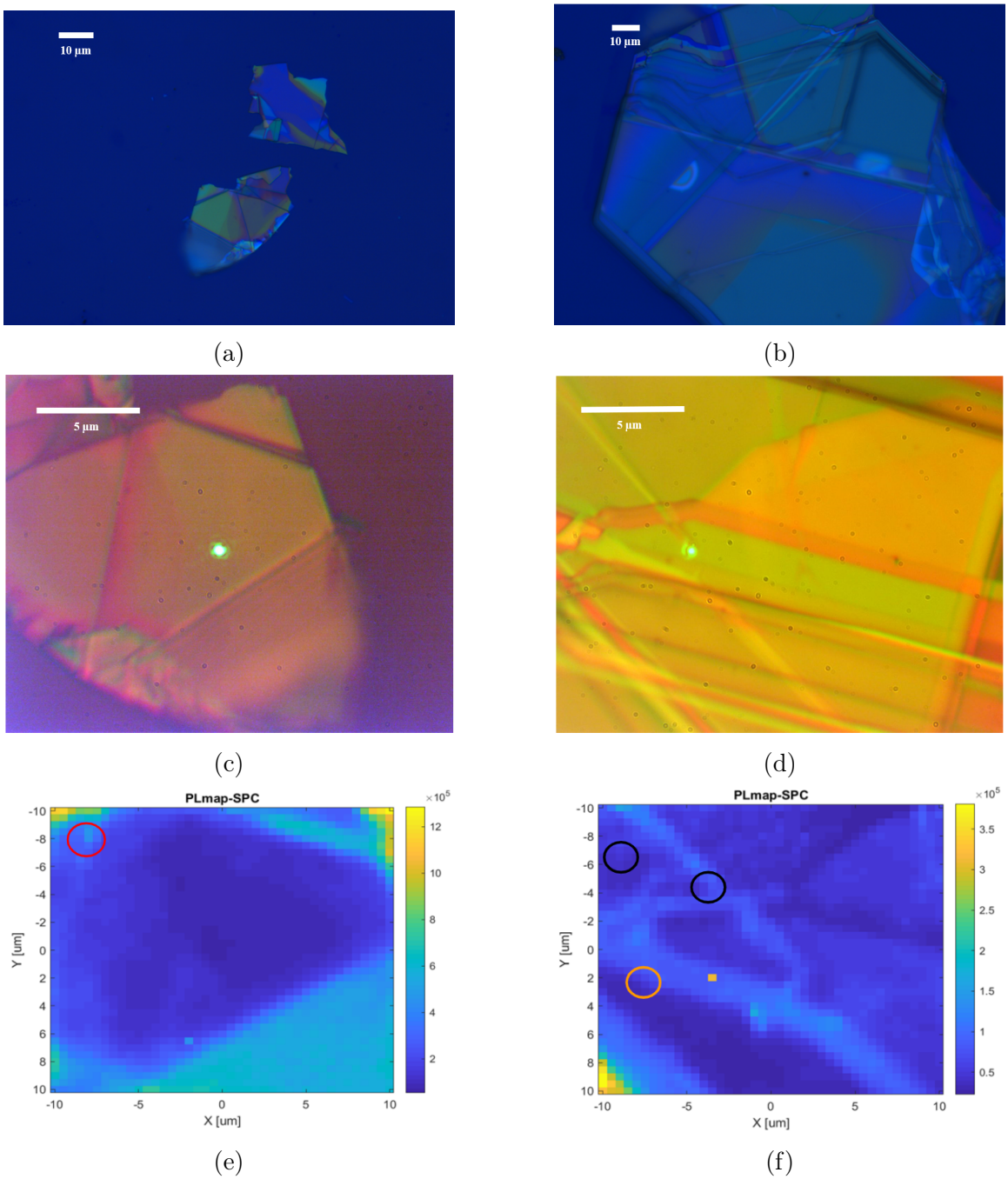

Figure 2-3: (a), (b): Optical microscope images of $hB^{10}N$ and $hB^{11}N$ (respectively) prior to collection of PL spectra. Approximate laser location shown, not to scale. (c), (d): Corresponding confocal microscope images with excitation laser shown. Diffraction results in a beam size of ≈ 1 micron. (e), (f): Corresponding $20\,\mu m \times 20\,\mu m$ PL maps. The laser in figures (c) and (d) are initially centered at (0, 0) in maps (e) and (f). Locations of SPEs are indicated by colored circles.

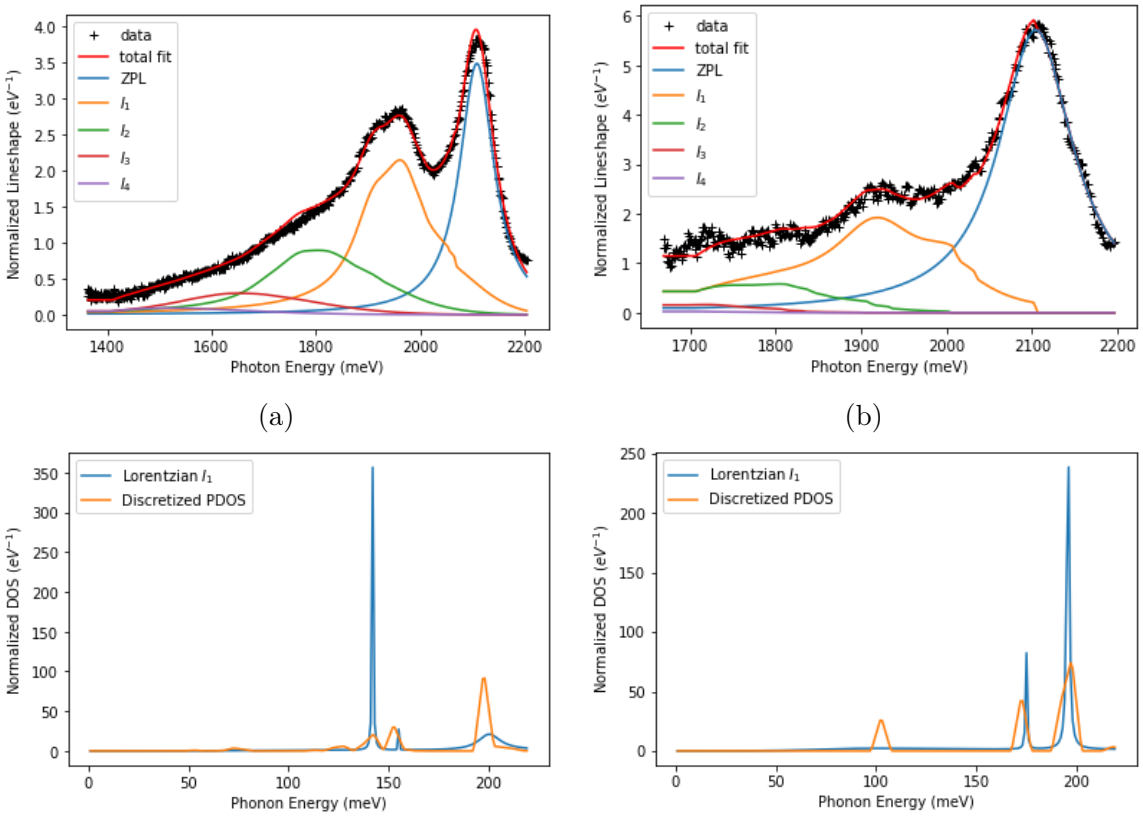

Figure 2-4: (a), (b): Fitted PL spectra for the SPEs indicated by the red and orange circles in Figures 2-3e and 2-3f. (c), (d): Corresponding PDOS for these two emitters.

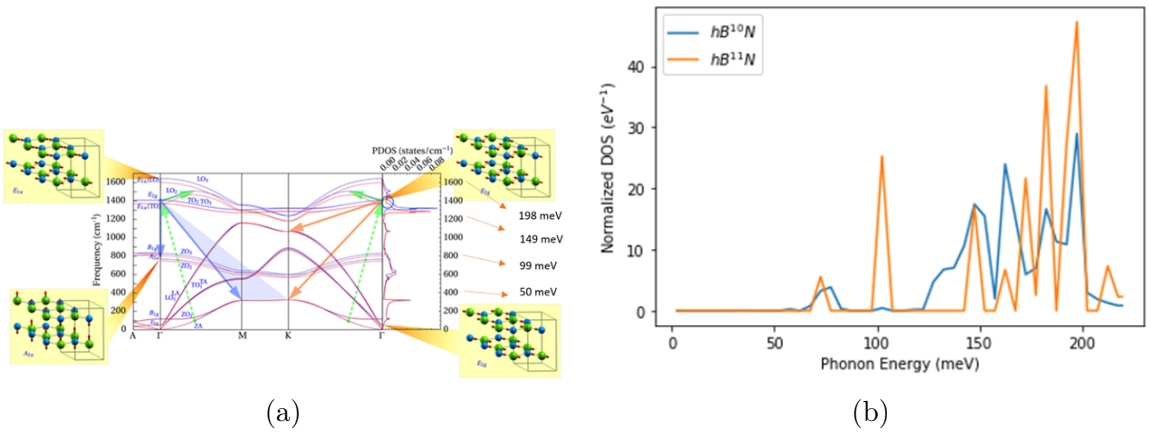

Figure 2-5: (a): Phonon dispersion curves and PDOS for $hB^{10}N$ (blue) and $hB^{11}N$ (red), as calculated in [3]. (b): Experimental predictions of PDOS for isopic hBN obtained by averaging the PDOS over all emitters.

Chapter 3

Semiconductor "Fock" Lasers

The content of this chapter is taken largely from my first author preprint last year [23].

3.1 Introduction

The generation of quantum states of light has long been a milestone of quantum optics. An example of such states are squeezed states, in which the uncertainty in one observable reduces at the expense of the other, An example of such variables are number and phase. States of light squeezed in photon number promise numerous applications in quantum information and sensing, allowing, for example, signal detection below the shot noise limit [4, 24]. In the limit of infinite number squeezing, one approaches a so-called Fock state, an energy eigenstate of the electromagnetic field Hamiltonian with a perfectly defined photon number n. In addition to their importance as fundamental quantum states of light, Fock states can be used to realize numerous quantum computing protocols that require operations on photon number (e.g., photon number subtraction and boson sampling) [25]. Thus, many applications would be aided by the generation of Fock or other highly number squeezed states.

Despite these potential rewards, macroscopic Fock and near-Fock states are inherently challenging to produce. The main reason for this is that there is a general lack of nonlinear mechanisms which selects specifically for n photons, especially where n

may be large. Moreover, most highly quantum states of light are difficult to maintain, due to the deleterious effects of loss.

To address these issues, the physical mechanism of nonlinear dispersive loss has been recently introduced as a potential new method to create "Fock" lasers, which possess steady state photon number distributions approaching macroscopic Fock states [26]. This phenomenon relies critically on the ability to simultaneously harness strong optical nonlinearities and low background loss (high Q cavities). Although the fundamental phenomenology of this effect has been developed, there are still large outstanding questions about potential platforms for realizing these new lasers.

One platform of potential interest for lasers which create strongly intensity squeezed light are semiconductor lasers. Semiconductor lasers have become ubiquitous due to their compact form factor, ease of electrical pumping, and wide gain bandwidths. There has already been considerable work on the topic of reducing noise in semiconductor lasers. The earliest methods for generating intensity-squeezed light with these devices involved exploiting the sub-shot noise regime of space charge limited current in diodes [27, 28]. In these demonstrations, reduced photon number noise and increased phase noise were obtained in constant current-driven semiconductor lasers. However, reducing pump noise was shown to reduce intensity noise by at most a few dB. Since these early works, attempts have been made to combine pump noise suppression with optical feedback using amplitude-phase decorrelation [29, 30, 31]. Still, relative intensity noise suppression did not surpass 10 dB, was limited by the linewidth enhancement factor α_L, and only appreciable for frequencies below the relaxation oscillation frequency. Because these methods achieve non-negligible squeezing in only part of the intensity noise spectrum, the total variance in photon number is weakly squeezed at best. Building off constant current driving, recent theoretical work has also considered exploiting pump electron antibunching ("quiet" pumping) to yield intensity noise squeezing [32]. However, significant squeezing will require sources of very strongly antibunched electrons and likely nanoLED platforms with near-unity spontaneous emission factors (incoherent output). To use semiconductor lasers in on-chip quantum sensing far below the shot noise limit and in quantum computing

protocols, enhanced squeezing is warranted.

Here, I show how semiconductor lasers with a strong and frequency dependent outcoupling could be used to create strongly intensity squeezed light with broadband squeezing of 10 dB or more below the shot noise limit. Additionally, I show that semiconductor lasers with strong carrier nonlinearities in conjunction with dispersive loss can exhibit a new kind of carrier bistability. I show how strong carrier nonlinearity can drastically impact laser steady state behavior, and also show how strong noise reduction can still be achieved even in the presence of this effect. Semiconductor lasers are a strong candidate platform to realize these effects due to their ability to sustain wavelength modulation owing to wide gain bandwidth and also possibly due to strong nonlinearities owing to smaller active regions like quantum wells. They are also amenable to on-chip integration with optical elements such as low loss resonators, photonic crystals, and lithium niobate optics, making them suitable for potential applications in quantum information and sensing [33].

3.2 Nonlinear dispersive loss and the concept of a "Fock laser"

In this section, I introduce and describe the operation of a "Fock laser" which can produce laser cavity states far below the shot noise limit, even approaching Fock states in extreme cases. The essential elements of a Fock laser are: (a) a pumped gain medium, (b) Kerr nonlinearity which gives the laser cavity an intensity dependent frequency shift, and (c) a frequency dependent outcoupling mechanism which gives the laser cavity a frequency dependent loss rate (Fig. 1a).

I first describe how under the right conditions, the combination of Kerr nonlinearity and frequency dependent loss lead to a laser cavity with an effective *intensity dependent loss* that controls the quantum state of light produced by the laser. Consider the cavity architecture shown in Fig. 1a, but without any gain medium. Additionally, I focus on a single cavity mode, with annihilation operator a. As is

well known, a cavity containing a Kerr nonlinearity develops an intensity dependent resonance frequency due to the intensity dependent index of the Kerr material. More specifically, the resonance frequency takes the form $\omega(n) = \omega_0(1 - \beta n)$, where ω_0 is the bare cavity frequency, and β is a dimensionless per-photon nonlinearity.

In addition to this Kerr nonlinearity, the cavity contains a frequency dependent outcoupling mirror characterized by the complex transmission amplitude coefficient $t(\omega)$ (associated with the intensity transmission coefficient $T(\omega) \equiv |t(\omega)|^2$). This frequency dependence can come from, for example, a Bragg reflector, or a Fano resonance which gives a Lorentzian reflectivity spectral profile. This frequency dependent outcoupling results in a corresponding frequency dependent damping rate in the cavity. Assuming $t \ll 1$, the frequency dependent damping rate of the cavity is given as $\kappa(\omega) \approx \mathrm{FSR} \cdot T(\omega)$.

When combined, the intensity dependent resonance frequency and frequency dependent dissipation give the cavity mode an effective *intensity dependent dissipation*. The one critical assumption for this description is that the temporal response of the frequency dependent mirror is fast compared to the round trip time of the cavity. This corresponds to an adiabatic limit in which the loss rate is able to near-instantaneously follow shifts in the cavity frequency caused by the Kerr nonlinearity. When these assumptions are fulfilled, the cavity field is subject to an effective intensity dependent damping rate $\kappa(n)$. Sharply frequency dependent reflectivity profiles enable the dissipation rate $\kappa(n)$ to take on forms which are highly nonperturbative in n, making this type of nonlinear dissipation fundamentally different than the types of nonlinear dissipation realized by multi-photon absorption. The fact that loss can vary sharply with photon number is fundamental to enabling the strong laser noise condensation I describe below.

I now describe how this intensity dependent loss can compress steady state photon statistics (Fig. 1b). The steady states of all lasers are characterized by a balance between saturable gain and loss. Gain saturation is itself a form of "intensity dependent gain," in the sense that the net gain seen by the cavity field depends on the intensity. Quantum mechanically, this means that different photon number states experience

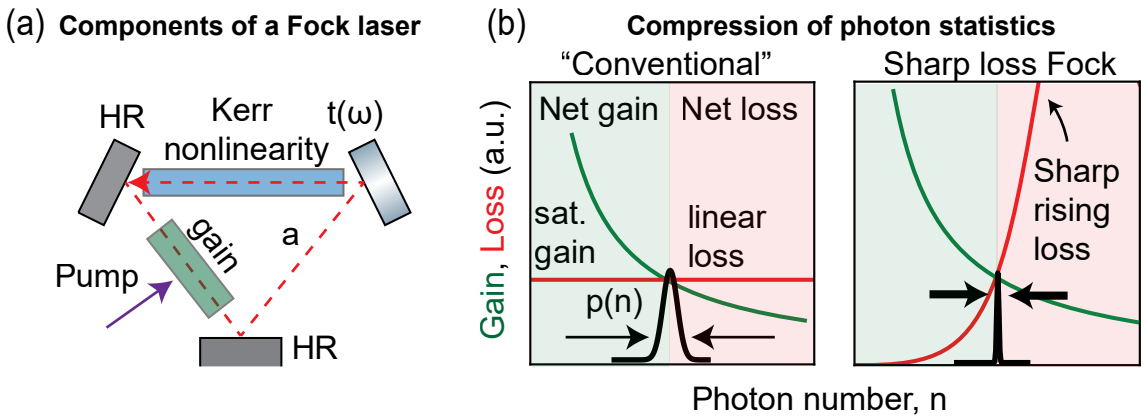

Figure 3-1: **The concept of a Fock laser.** (a) Essential components of a Fock laser (illustrated as a ring laser for concreteness) consisting of at least one mirror with frequency dependent transmission $t(\omega)$. (b) Comparison of conventional and sharp loss Fock laser steady state photon probability distribution $p(n)$. The steady state photon number is determined by the location of intersection between saturable gain and loss. The variance of the probability distribution is determined by the effective "steepness" of intersection of the gain and loss curves. While the conventional laser architecture with linear loss results in a near-coherent state far above threshold, the sharp loss architecture results in states with variance below the mean, which correspond to non-classical light. In the most extreme limit, this mechanism can enable the generation of near-Fock states inside the laser cavity.

different amounts of gain. In a conventional laser with intensity independent "linear loss," the loss rate seen by the cavity field is the same for all photon numbers. For photon numbers where gain exceeds loss, an effective "force" encourages occupation of yet higher photon numbers; for photon numbers where loss dominates gain, an effective force encourages occupation of lower photon numbers. The intersection point where "gain equals loss" represents the equilibrium point between these two forces, and consequently determines the mean photon number of the cavity in the laser steady state. While the intersection point determines the mean photon number, the behavior of the photon number dependent gain and loss in the vicinity of this intersection dictates the variance of the photon number probability distribution $p(n)$. In conventional lasers which are far above threshold, the probability distribution approaches that of a coherent state, with Poissonian statistics (variance equal to the mean). It is this fact that leads to the common statement that "lasers produce coherent states."

This situation changes significantly if the number dependent gain or loss profiles deviate substantially from their usual forms. I will focus here on situations where the gain remains identical, but the ordinary linear loss is replaced with a strongly intensity dependent loss. If the loss rises sharply with photon number around its intersection with the saturable gain, then the steady state probability distribution becomes compressed compared to the case of linear loss. To understand this, I can return to the picture of "forces" on the probability distribution described for the normal laser. The magnitudes of these forces are essentially determined by the extent to which gain exceeds loss (or vice versa) below (or above) the mean photon number. Comparing the conventional and sharp loss lasers, it is clear that above the mean photon number, loss exceeds gain more aggressively for the sharp loss. Since loss dominates gain more strongly, the probability distribution is more strongly "discouraged" from entering this region. The result of this is that the probability distribution has the same mean, but can become strongly compressed, resulting in a much lower variance. Roughly speaking, the mean photon number is determined by the location of the intersection point, while the variance is determined by the ratio of the slopes of the gain and loss.

This mechanism enables the sharp loss laser to create steady states with variance lower than the mean, a feature only possible in non-classical light. In the most extreme limit, the loss rises so sharply that only a single number state (the mean) has a substantial probability of occupation, resulting in a cavity Fock state.

3.3 Semiconductor Fock laser architecture

In this section, I introduce the semiconductor "Fock laser" architecture that generates strongly noise condensed steady states inside the optical cavity. The device is a semiconductor heterostructure with an electrically pumped active region (Fig. 3-2a). The cavity mode (with annihilation operator a) has a bare resonance frequency ω_0. One of the end facets is a broadband reflector, while the other is a sharply dispersive element, such as a Fano resonance structure (main text) or a Bragg reflector

(Appendix), which equips the cavity with sharply frequency dependent dissipation. Both Kerr and carrier nonlinearity inside the cavity shift the index, and hence the resonance frequency (Fig. A-2b). However, as I show in Section 3.4.3, the effect of these two nonlinearities on photon quantum statistics is very different.

To lowest order, the cavity frequency depends linearly on the photon and inverted carrier numbers n and N as

$$\omega(n, N) = \omega_0(1 - \beta n - \sigma N), \tag{3.1}$$

as analyzed previously using coupled mode theory and supported experimentally [34, 35, 36, 37]. The dimensionless, per-photon Kerr nonlinear strength β is related to the Kerr nonlinear coefficient n_2 (m^2/W) via $\beta = -\frac{\hbar\omega n_{\mathrm{eff}}^2 n_2 c}{8V_m}$, where V_m denotes the modal volume, n_{eff} the cavity's effective refractive index, and ω the laser frequency. The carrier nonlinearity σ is material-dependent and is directly related to the linewidth enhancement factor, as described in the Appendix. It arises predominantly from two-photon absorption, band filling effects, and free carrier dispersion.

Here, I consider a semiconductor laser with separate gain and Kerr nonlinear elements. I choose to use a different material for the Kerr nonlinearity in order to avoid possible dispersive resonant effects of optical nonlinearity near transition energies in the gain material. The Kerr material is still chosen to be a GaAs-based semiconductor due to its strong optical nonlinearity from bound carriers. I describe Fock lasers based on "active nonlinearity" (in which the gain and Kerr materials are the same) in the Appendix, emphasizing that the timescale of resonant effects in that case may invalidate the assumption of the cavity resonance frequency's instantaneous response to changes in photon number.

By enlarging the volume of the Kerr nonlinear chip relative to the gain chip, the optical nonlinearity of the cavity is dominated by the nonresonant Kerr nonlinearity of the former. This assumes the modal volume is approximately uniform across the two materials with minimal loss at the interface (i.e. the gain and Kerr materials should be index matched). Then, the effective Kerr nonlinearity of the cavity is given

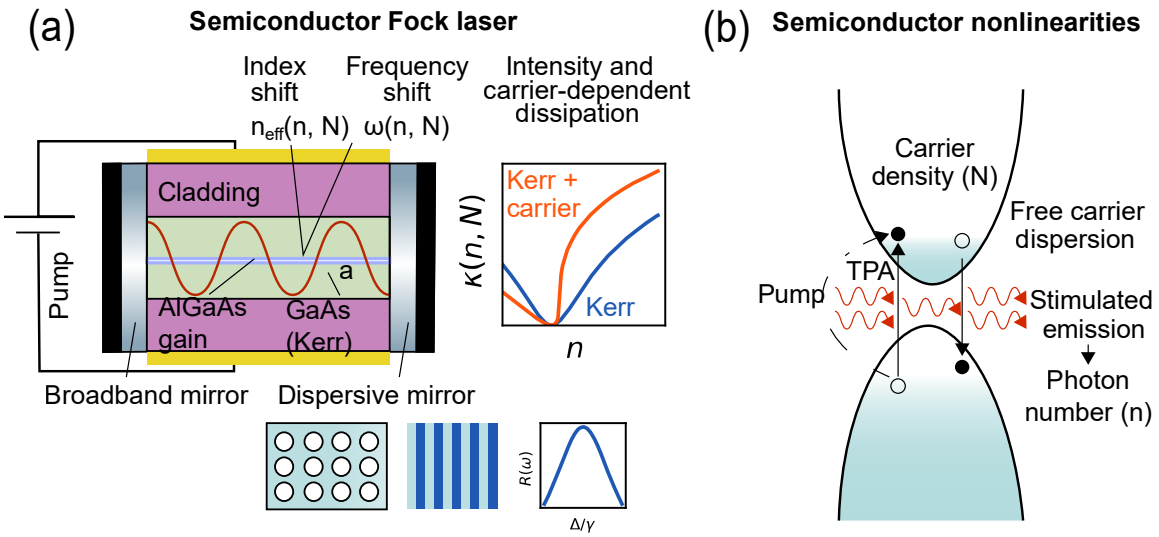

Figure 3-2: **Semiconductor Fock laser architecture with separate gain and Kerr elements**. (a) Basic semiconductor laser diode heterostructure design with nonlinear dispersive loss. Dispersive outcoupling is generated via the sharp frequency dependent transmission of a photonic crystal element. Coupling of Kerr nonlinearity from the Kerr material and carrier nonlinearity from the gain material with dispersive loss $R(\omega)$ creates sharp nonlinear loss $\kappa(n, N)$. Here, Δ denotes detuning from the dispersive (Lorentzian) resonance and γ denotes the width of the dispersive resonance (related to its FWHM). (b) Semiconductor optical nonlinearities, including intensity dependent Kerr effect as well as carrier-dependent free carrier dispersion (FCD) and two photon absorption (TPA). These nonlinearities shift the real part of the cavity's refractive index, in turn shifting the resonance frequency in the diode cavity. Weak nonlinear loss from shifting the imaginary part of the refractive index via the Kramers-Kronig relations is also generated, but in most cases is negligible compared to the nonlinear dispersive loss.

by $\beta_{\text{eff}} \approx x\beta_a + (1-x)\beta_p$ where nominally the active region filling factor $x \ll \beta_p/\beta_a$ so that the passive Kerr nonlinearity β_p dominates over the active one (β_a). This allows the refractive index, and thus resonance frequency, to respond instantaneously to changes in photon number, relative to other timescales in the system.

Following the same reasoning of the previous section, the photon and carrier number dependence of the resonance frequency can transfer to the loss, so long as the cavity resonance frequency responds instantaneously to changes in both photon and carrier number. In this case, the carrier and photon number dependent loss is given by

$$\kappa(n, N) \equiv \kappa(\omega(n, N)) = -\text{FSR} \cdot \log R(\omega(n, N)), \tag{3.2}$$

where in the limit of a small gain chip and large Kerr chip, the resonance frequency just depends on photon number through the Kerr nonlinearity, $\omega(n, N) \to \omega(n)$.

Hence the sharp frequency dependent element with reflectivity $R(\omega)$ now controls the nonlinear loss. As I will show, these systems can provide new behaviors not just in their steady states, but also through new quantum noise behaviors.

3.3.1 Semiconductor Laser Dynamics

Semiconductors typically fall into the category of so-called "class B" lasers, in which the polarization dynamics decay quickly relative to the timescales associated with carrier recombination and cavity decay. In this case, the polarization dynamics are adiabatically eliminated, resulting in Heisenberg-Langevin equations for photon number, carrier number operators, and phase [38]:

$$\dot{n} = (G(n, N) - \kappa(n, N))\, n + F_n \tag{3.3a}$$

$$\dot{N} = I - \left(nG(n, N) + \gamma_\parallel N\right) + F_N \tag{3.3b}$$

$$\dot{\phi} = -\omega(n, N) \tag{3.3c}$$

$$= \frac{\alpha_L}{2} G(n, N) + \beta n + F_\phi \tag{3.3d}$$

To be maximally general here, I allow the gain G and loss κ to depend on both the carrier density N and photon number n (the latter could account for gain saturation). In writing this form of the gain and loss, I have assumed that the gain and loss respond effectively instantaneously to changes in the photon and carrier number. Pumping is performed by carrier injection using current I (in units of carrier density per unit time), and $\gamma_\parallel$ denotes the nonradiative decay rate of carriers. Furthermore, α_L denotes the linewidth enhancement factor and is associated with amplitude-phase coupling. The decay rates are associated with Langevin force terms $F_{n,N,\phi}$ with nonzero correlators given by the diffusion coefficients (including the effects of TPA, $\dot{n} = -\alpha_{\mathrm{TPA}} n^2$): $\langle F_n^\dagger F_n \rangle = \langle 2D_{nn} \rangle = 2R_{sp} n + \alpha_{\mathrm{TPA}} n^2, \langle F_N^\dagger F_N \rangle = \langle 2D_{NN} \rangle = 2(R_{sp} n + \gamma_\parallel N), \langle F_N^\dagger F_n \rangle = \langle 2D_{NN} \rangle = -Rn, \langle F_\phi^\dagger F_\phi \rangle = \langle 2D_{\phi\phi} \rangle = R_{sp}/2n$ where $R_{sp} \approx G(n, N)$

denotes the rate of spontaneous emission into the cavity mode, $R_{abs} \approx 0$ denotes the rate of absorption (negligible above threshold), and $R = R_{sp} + R_{abs}$. These correlators give rise to nonzero fluctuations in n, N about their steady state values. A derivation of $\langle 2D_{nn} \rangle$ including the effects of TPA is provided in the Appendix.

In all examples presented in the main text, I consider linear gain neglecting saturation effects, $G(n, N) = G(N) = G_N(N - N_{\text{trans}})$ with N_{trans} the transparency carrier density. I found no significant differences using logarithmic quantum well gain or including the effects of gain saturation [39].

3.3.2 Noise properties

The steady state noise properties of semiconductor lasers can be computed by considering operator valued fluctuations of the Heisenberg-Langevin equations from their mean solutions. In the steady state, this results in a pair of coupled linear equations for the operator values fluctuations δn and δN, which are given as:

$$\begin{bmatrix} \delta\dot{n} \\ \delta\dot{N} \end{bmatrix} = M \begin{bmatrix} \delta n \\ \delta N \end{bmatrix} + \begin{bmatrix} F_n \\ F_N \end{bmatrix}$$

with the fluctuation matrix

$$M = \begin{bmatrix} -n\kappa_n & n\,(G_N - \kappa_N) \\ -G_0 & -(nG_N + \gamma_\parallel) \end{bmatrix}$$

Here, for example, $\kappa_n = -\beta\omega_0\kappa_\omega = -\beta\omega_0(d\kappa/d\omega)$ represents the sharpness of the dispersive loss, with the instantaneous laser frequency being given by $\omega(n, N)$.

By solving this linear system in the frequency domain, one can construct the frequency resolved power spectrum of fluctuations for either of the operators. Of particular interest is the photon number variance, given by $(\Delta n)^2 = \frac{1}{\pi}\int_0^\infty \langle \delta n^\dagger(\omega)\delta n(\omega)\rangle$. The fluctuation spectrum inside the integral is related to the frequently defined relative intensity noise (RIN) as

$$\text{RIN} = \frac{1}{n^2}\langle \delta n^\dagger(\omega)\delta n(\omega)\rangle, \tag{3.4}$$

A useful parameter to quantify the quantum nature of light is the Fano factor, defined as $F = (\Delta n)^2/n$. The Fano factor is 1 for Poissonian light, corresponding to the shot noise limit; values below one indicate sub-Poissonian light below the show noise level. I calculate the most general expression for F in the presence of nonlinear dispersive loss in the Appendix.

Here, I summarize the results corresponding to a few important limiting cases where the effect of amplitude-phase coupling on intensity noise may be neglected.

For completeness, I include the effect of two-photon absorption (TPA) when considering carrier nonlinearities (two-photon carrier generation is negligible compared to the pump current). However, for most systems, the magnitude of dispersive loss is at least an order of magnitude greater than TPA-induced loss; the effects of TPA are only seen at the weakest nonlinearities and lowest background losses. A more thorough discussion of TPA is provided in the Appendix. Important physical parameters to characterize intensity noise are the relaxation oscillation frequency and damping rate of relaxation oscillations. As derived in the Appendix, these are respectively given by

$$\Omega_R^2 \approx (nG_N + \gamma_\parallel)(n\kappa_n) + n(G_N - \kappa_N)\kappa$$
$$\Gamma_1 \approx n(G_N + \kappa_n) + \gamma_\parallel$$

These measures provide an important way to understand the effect of nonlinear dispersive loss on intensity noise. The limiting Fano factors are thus:

1. For weak Kerr and carrier nonlinearities, $\kappa_n, \kappa_N \to 0$, I have $F \to 1 + \kappa/(nG_N)$ when pumping far above threshold, recovering linear behavior. When n becomes large far about threshold, the Fano factor approaches 1, resulting in Poissonian (coherent) statistics.

2. For strong Kerr nonlinearity but weak carrier nonlinearity, $n|\kappa_n| \gg \kappa_0, n|\kappa_N|, \gamma_\parallel, G_N$, the Fano factor $F \to \kappa/|n\kappa_n|$ for large n. Critically, the ratio $|\kappa_n|/\kappa$ is a measure of how sharply the loss varies with n compared to the absolute loss rate at the

steady state photon number, and thus dictates the dimensionless "sharpness" of the loss. The Fano factor is inversely proportional to this sharpness factor, and thus sharp losses lead to sub-Poissonian states.

3. For strong carrier nonlinearity but weak Kerr nonlinearity, $n|\kappa_N| \gg \kappa_0, n|\kappa_n|, \gamma_\parallel$, I have $F \to \kappa/(nG_N) + G_N/|G_N - \kappa_N| \to G_N/|G_N - \kappa_N|$ for large n. The carrier nonlinearity reduces dependence of the rate of change of intensity fluctuations on carrier fluctuations ($G_N \to G_N - \kappa_N$), lowering the relaxation oscillation frequency Ω_R^2 while leaving the damping of these oscillations unchanged. This can amplify low-frequency intensity noise slightly.

4. For simultaneously strong Kerr and carrier nonlinearities, $n|\kappa_{n,N}| \gg \kappa_0, \gamma_\parallel$,

$$F \to \frac{\kappa}{n|G_N + \kappa_n|}\left(1 + \frac{nG_N^2}{n\kappa_n G_N + |G_N - \kappa_N|\kappa}\right). \tag{3.5}$$

Roughly, this expression can be broken into Kerr nonlinearity (first term) and carrier nonlinearity (second term) contributions. The former describes squeezing via increased Ω_R^2 and damping of relaxation oscillations due to "sharp" intensity dependent loss, while the latter reduces intensity noise-carrier noise coupling and thus Ω_R^2. Kerr and carrier nonlinearities may therefore have competing effects, leading to interesting steady state and noise fluctuation behavior.

3.3.3 Example setup parameters

I emphasize that measured nonlinear strengths can vary widely based on experimental conditions, but to provide a rough estimation of typical per-photon Kerr nonlinearities for the parameters considered here, I note order-of-magnitude values for bulk (active region volume $V \approx 10^{-16}$ m^3) and QW/QD semiconductors (active region volume $V \approx 10^{-18} - 10^{-17}$ m^3), employing passive (below bandgap) or active (above bandgap) Kerr nonlinearity, in Table 3.1. Values are calculated from data summarized in an earlier review of nonlinear refraction in semiconductors [40]. Note that stronger nonlinearities may be accessible using InGaAs- or AlGaAs-based materials.

Table 3.1: Order-of-magnitude estimates of per-photon Kerr nonlinearities (β) in GaAs-based semiconductors at active and passive wavelengths, for typical diode and photonic crystal (PC) lasers.

	Bulk GaAs diode laser	GaAs-based QW diode laser[1]	GaAs-based QW PC laser
Passive	-10^{-11} (1.5 μm)	-10^{-10}	-10^{-9}
Active	10^{-4} (873 nm)	10^{-3}	10^{-2}

For active nonlinearities, I point out again that large values of β are also generally associated with slow response times, which may be too slow for the version of nonlinear dispersive loss presented here to be effective, or significant absorptive loss. Detuning the cavity away from resonance would result in weaker, more instantaneous nonlinearities compatible with the nonlinear dispersive loss mechanism, still with considerable intensity noise condensation. Note also that the sign of β just changes which side of the nonlinear dispersive resonance sharp loss ($\kappa_n > 0$) occurs, which is irrelevant for the symmetric Fano dispersive losses I consider in the main text.

For concreteness, I propose the following example system: a laser operating around 1.5 μm with gain medium InGaAs/InAlGaAs QWs and Kerr medium GaAs. Given the ratio of Kerr nonlinear coefficient n_2 for both materials, a geometrical enhancement such that $x \approx 10^{-4}$ is needed for the passive nonlinearity of GaAs to dominate β_{eff}. To minimize absorption loss, $Al_{0.18}Ga_{0.82}As$ may be used as the Kerr material instead, since it has similar n_2 but absorption losses over an order of magnitude lower than GaAs.

In this design, the Kerr nonlinear material dominates the refractive index (and resonance frequency) shifts. In the Appendix, I describe how small variations in steady state and noise behavior arise from other weak nonlinear effects such as two-photon absorption (TPA) and nonlinear gain saturation.

Unless otherwise noted, Figures in the main text use the following parameters for the designs proposed in Sec. **??**, chosen to be similar to experimentally determined parameters for GaAs-based lasers: modal volume and active region volume $V = 10^{-16}$ m^3 (confinement factor $\Gamma = 1$), bare cavity resonance frequency $\omega_0 = 2.16 \times 10^{15}$ s^{-1} (873 nm), free spectral range FSR = 17 GHz, transparency density $N_{\text{trans}} = 2 \times 10^{24}$

m^{-3}, nonradiative decay rate $\gamma_{\|} = 3 \times 10^8$ rad/s, and linear gain coefficient $G_N = 1/V \cdot dG/dN = 3694$ rad/s [41].

For quantum well gain, active region volumes are roughly one and two orders of magnitude below V for double heterostructure diode lasers and photonic crystal (PC) lasers, respectively. The latter is similar to the Fano laser structure considered in earlier works [42].

For sharp losses in the main text, I consider symmetric Fano loss profiles, with central frequency given by $\omega(n_c = 10^6, N_c = N_{\text{trans}})$ and resonance decay (FWHM) $\gamma = 2 \times 10^{12}$ rad/s.

3.4 Results

3.4.1 Noise condensation from Fano-based nonlinear loss

I now discuss how this semiconductor laser architecture with sharp nonlinear loss can lead to new behaviors in both the mean field as well as the fluctuations, eventually leading to strongly noise-reduced states. I begin by considering systems in the absence of carrier nonlinearity. In Fig. 3-3, I compare steady state and intensity noise plots for conventional linear loss and sharp (Lorentzian/symmetric Fano) loss. Linear loss presents an n-independent loss profile, and leads to the well known linear dependence of steady state photon number on pump current. In the presence of dispersive loss, moderate nonlinearity ($\beta = -10^{-10}$) begins to modify the steady state behavior. For pump currents just above threshold, the behavior is close to linear. However, as the pump current increases, so does the loss, pulling down the input-output curve to a sub-linear behavior. For even stronger nonlinearity ($\beta = -10^{-9}$), a bistable transition occurs that creates a range of photon numbers which have no stable steady state solution. In particular, this occurs because there is a nonzero photon number at which the cavity experiences minimum loss. This left bistable edge lies below threshold, and thus needs to be accessed "from above", by pumping to a high power (beyond the range of zero solutions), and slowly lowering the power (this is a hysteresis

effect).

Beyond the point of bistability (roughly 30 mA in Fig. 3b), n stays approximately constant while the photon number variance Δn^2 can decrease sharply. I see the consequence of this in Fig. 3-3c, which plots the Fano factor spectrum $n \cdot \mathrm{RIN} \equiv \Delta n^2(\omega)/n$. Here, the intensity noise fluctuations associated with relaxation oscillations are quenched closer to the bistable point. Due to the sharp loss, the relaxation oscillation peak is in general significantly suppressed compared to the case of linear loss. As a result of the bistability, the laser can exist in two states with very different photon numbers over a range of pump currents. The larger photon number branch corresponds to sharp loss ($\kappa_n > 0$) in this scheme. Overall, nonlinear dispersive loss creates significant broadband intensity noise squeezing by orders of magnitude compared to analogous linear loss.

Finally, I calculate Fano factors as a function of pump current in Fig. 3-3d by integrating the spectra in Fig. 3-3c. For linear loss, as the intracavity intensity grows with pump current, the relaxation oscillations shift to higher noise frequencies but also undergo stronger damping, giving rise to a decaying Fano factor that approaches the shot noise limit far above threshold. Stronger linear losses amplify relaxation oscillations but do not affect the shot noise limit.

The behavior of Fano factor for nonlinear dispersive loss is phenomenologically different. For simplicity, in Fig. 3-3d, I only plot the sharp loss (upper) branch when bistability is present (purple curve) [1]. On the upper branch, linear behavior (shot noise) is restored as the detuning from the Fano resonance grows large: this corresponds to low reflectivity, high loss, and high pump currents. Approaching the left bistable edge, the cavity frequency approaches the Fano resonance and, for a certain n, the ratio $\kappa/(n\kappa_n)$ approaches a minimum, corresponding to minimum Fano factor. The Fano factor does not decrease indefinitely approaching the left bistable edge. Coupling of intensity and carrier density implies that even at zero loss, nonzero carrier noise and thus intensity noise exist due to the nonradiative decay $\gamma_\parallel$. This

[1] The lower branch, accessible by normal pumping from threshold, resembles linear behavior apart from the bistable point, which creates a discontinuity in the Fano factor as a function of pump current.

results in an increase of Fano factor at the left bistable edge. Nonetheless, nonlinear dispersive loss creates a range of pump currents over which intensity noise drops far below the shot noise limit. The effect is stronger for lower linear background losses and larger (Kerr) nonlinearities, with a maximum of 92% (12 dB) reduction in Fano factor below the shot noise limit displayed in Fig. 3-3d.

3.4.2 Noise condensation using nonlinear distributed feedback-based loss

In this section, I consider distributed feedback semiconductor lasers where a distributed Bragg reflector (DBR) is fabricated on one (or both) ends/facets of the laser cavity, or a VCSEL-type structure is employed. In this case, I use Eq. 3.2 with the analytical form for reflectivity given by coupled mode theory [43, 44] to obtain

$$\kappa(\omega) = -\mathrm{FSR} \cdot \log \left| \frac{g \sinh(\theta)}{\Gamma \cosh(\theta) + (\alpha_{\mathrm{DBR}} + i\delta) \sinh(\theta)} \right|^2, \tag{3.6}$$

where $\beta = \tilde{n}\omega/c$ is the propagation constant (wavevector), $g = \omega \Delta n/(\pi c)$ is the approximate coupling coefficient, $\delta = \beta - \pi/d$, $\Gamma^2 = g^2 + (\alpha_{\mathrm{DBR}} + i\delta)^2$, $\theta = N_{\mathrm{DBR}} d\Gamma$, and α_{DBR} the radiative loss from the DBR. Here, N_{DBR} denotes the number of pairs of layers in the DBR, d the thickness of a pair of layers, Δn the index contrast, $\tilde{n}$ the effective index, and $\omega \equiv \omega(n, N)$ the laser frequency. Note that δ has the interpretation of a detuning from the Bragg value π/d (the center of the Bragg stop-band of maximum reflectivity and thus lowest loss is at $\delta = 0$). I would like to operate in the "sharp loss" regime, which is where the stop-band switches over to a pass-band, first occurring when $\theta = \pi \implies \delta^2 - g^2 = \pi^2/L^2$. For a lossless DBR, choosing the frequency ω_c at which this sharp transition occurs fixes δ and therefore Δn from the above relations:

$$\Delta n = \frac{\pi c}{\omega_c} \sqrt{\left(\frac{\tilde{n}}{c} (\omega_c - \omega_t) \right)^2 - \left(\frac{\pi}{L} \right)^2}, \tag{3.7}$$

where ω_t denotes the center of the stop band, so that $\omega_c - \omega_t$ is effectively the half-

width of the stop band. The coupling coefficient g, index contrast Δn and stop band width $2(\omega_t - \omega_c)$ are thus closely related.

To use Eq. 3.6, it is necessary to ensure the time response of the DBR is much faster than the free spectral range. I extract this time response by performing an FFT of $R(\omega)$. For lossy DBRs, $R(\omega)$ approaches a Lorentzian with width governed by α_{DBR}, and the maximum reflectivity may be far from unity. When the DBR is lossless, an analytical expression for the time response is in general difficult to obtain. I observe that the time response is faster for DBRs of larger bandgap (wider stop bands). Intuitively, outcoupling in a lossless DBR is through the coupling coefficient g which scales with the index contrast Δn and thus correspondingly with the stop band width $2(\omega_c - \omega_t)$. This is distinct from the Fano resonances considered in the main text where the loss profile was derived from interference between a "direct channel" pathway bypassing the Fano resonance and an "indirect pathway" coupling to an intrinsic resonant mode of the photonic crystal. In such a case, the time response of the effective nonlinear dispersive loss is governed by the the complex resonance frequency of the Fano resonance (intuitively, how long light spends trapped in the photonic crystal). Here, however, sharply frequency dependent loss arises from a different mechanism, namely the photonic bandgap of the DBR.

I explore coupling of a Kerr nonlinearity with an approximately lossless DBR in Fig. 3-5 with linear background loss $\kappa_0 = 10^{-1} \cdot \mathrm{FSR}$ ($Q \approx 2 \times 10^5$). Furthermore, I fix the position of the stop band in photon number, though the values of $\omega_{c,t}$ vary with nonlinear strength. From $\omega_{c,t}$ and the DBR length, I calculate the required index contrast Δn via Eq. 3.7.

I first examine steady state behavior. The sharpness of $\kappa(n)$ increases with the number of layers N_{DBR} and Kerr nonlinear strength (the former corresponds to sharper evanescent decay of modes in the photonic bandgap), as shown in Fig. 3-5a. For the strongest nonlinearity and sharpest $R(\omega)$, multiple stop bands may be accessible, corresponding to multiple regions of noise condensation. Input-output S-curves are shown in Fig. 3-5b, demonstrating bistability for each transition from pass band to stop band. An important distinction from the Fano resonances considered earlier is

that the sharp loss regions $\kappa_n > 0$ are now the lower bistability branches, accessible by simply pumping smoothly from threshold. Finally, I investigate the integrated Fano factor.

For the sharpest losses, I reach nearly 20 dB squeezing below the shot noise limit ($F \approx 0.02$). I plot here only the lower bistable branch, though for large pump currents, the laser would cross a bistable point and either enter a linear loss regime (orange curves) or a second bistability region (solid blue curve).

From an experimental standpoint, the sharpest loss (and strongest squeezing) can be obtained by maximizing the stop band width and number of layer pairs N_{DBR}. The former is limited by the intracavity saturation intensity and required index contrast Δn, while the latter is limited by fabrication methods. Nevertheless, carefully-engineered DBR-based losses when coupled to strong Kerr nonlinearity in semiconductor lasers may result in unprecedented broadband intensity noise squeezing.

3.4.3 Bistability from carrier nonlinearity

In this section, I describe how the interplay of carrier nonlinearity with dispersive loss can result in unexplored "carrier bistability" behavior. I consider carrier nonlinear strengths σ comparable to what they might be in, for example, GaAs-based gain media [45, 37].

I first describe how multiple lasing steady states can exist when strong carrier nonlinearity and dispersive loss are simultaneously present. In an ordinary semiconductor laser, the "gain equals loss" requirement leads to a so-called "gain clamping" condition, wherein above threshold, the inverted carrier density is fixed at some value, regardless of the intensity (i.e. the carrier density N such that $G_N(N - N_{\mathrm{trans}}) = \kappa$). This is depicted in Fig. 3-4a by the "linear loss" case which shows only a single intersection point of the carrier dependent gain and carrier independent loss. However, in the presence of strong carrier nonlinearity and sharply frequency dependent outcoupling (with a Fano mirror for example), the loss of the cavity mode can depend nonlinearly on the carrier density N, $\kappa(\omega(N)) = \kappa(N)$. As the carrier density changes, so does the cavity frequency, and hence the damping rate via the frequency dependent mirror.

The "gain equals loss" condition now reads $G_N(N - N_{\text{trans}}) = \kappa(N)$. As shown in Fig. 3-4a, this leads to a situation where more than one carrier density N can cause gain and loss to be equal, corresponding to multiple cavity resonance frequencies. In the case of the Fano resonance, I see that up to three different steady states are possible.

Fig. 3-4b shows how this phenomenon manifests in the steady state laser behavior. The dependence of steady state intensity on the pump current is still linear, but there can be up to three independent branches, corresponding to different steady state N and different lasing frequencies. For the Fano mirror example, one resonance frequency is always present such that the detuning from the Fano resonance $\Delta \approx 0$. Since this solution has lowest loss, and thus the lowest threshold, lasing will occur here by default. The other branches are also stable, but disconnected from the lowest branch. It may be possible to experimentally access these higher branches through dynamic pumping schemes which generate transients that can travel from one branch to another.

When Kerr nonlinearity is also introduced, additional phenomena appear due to the simultaneous nonlinear dependence of the damping rate on intensity and carrier number. It is important to note that the profile $\kappa(\omega)$ is unchanged, though $\kappa(n, N)$ will vary based on the nonlinear strengths. Furthermore, the gain (and thus loss) is monotonically increasing in N. For typical materials (and for the results presented in Fig. 3-4), $\sigma < 0$ increases the resonance frequency $\omega(n, N)$ and thus pushes lasing solutions rightward along $\kappa(\omega)$.

Consider first weak carrier nonlinearity (orange and green curves in Fig. 3-4c). Then, the carrier nonlinearity can be treated as a perturbation to the initially symmetric Lorentzian loss $\kappa(n)$. On the $\kappa_\omega \equiv d\kappa/d\omega > 0$ (right) branch of the dispersive loss, the carrier nonlinearity shifts the loss curve upward. On the other hand, the $\kappa_\omega < 0$ (left) branch shifts downwards since an increase in ω corresponds to a point of lower loss (approaching detuning $\Delta = 0$).

Suppose I increase the carrier nonlinearity further (red curve in Fig. 3-4c). For n near threshold, far below the "magic" photon number $n_c \approx 10^6$ of lowest loss, the carrier nonlinearity pushes solutions rightward along the Lorentzian. However, the

laser still lies on the $\kappa_\omega < 0$ branch - the carrier nonlinearity pushes the mode closer to n_c, which is near zero loss and thus $N \approx N_{\text{trans}}$. This yields one steady state solution. For higher n, near but still below n_c, I eventually reach an n at which two solutions are possible: $N \approx N_{\text{trans}}$ (lower loss) or $N > N_{\text{trans}}$ (higher loss). Immediately afterwards, a third solution is possible with still higher loss/higher carrier density, phenomenologically similar to the dashed curve in Fig. 3-4a. Finally, as κ_ω drops past the inflection point of $\kappa(\omega)$, a point corresponding to two solutions marks the end of the carrier bistability and for the largest n I again obtain only one solution (the Lorentzian loss looks approximately linear).

For even stronger carrier nonlinearity (purple curve in Fig. 3-4c), the carrier bistability boundaries shift leftward in photon number. Comparing the red and purple curves in Fig. 3-4c, the left boundary eventually crosses zero and becomes negative, at which point the loss curve detaches into two parts: a sharp part at low loss and linear part at higher loss, separated by a range of pump currents over which no stable lasing solution occurs. When the right bistability boundary also crosses $n = 0$ the sharp loss vanishes and laser operation only occurs on the linear high-loss branch (with correspondingly larger threshold currents), as shown for the brown curve in Fig. 3-4c.

I now examine the effects of this carrier bistability on intensity noise. As shown in Fig. 3-4e, the minimum achievable Fano factor is relatively independent of the level of carrier nonlinearity. This can be seen by noting that the first term in Eq. 3.5 dominates the Fano factor at these points. However, past the sharp loss region, the linear branch created by the carrier nonlinearity possesses a higher loss that pulls the Fano factor upward for larger pump currents. For large carrier nonlinearities, the system eventually hits bistability and a region of unstable lasing, transitioning to (approximately) linear behavior again. For carrier nonlinearities much stronger than the Kerr nonlinearity (brown curve), approximately linear loss is restored as described above and no intensity noise reduction is observed. Mathematically, Eq. 3.5 essentially contains a combination of dominant Kerr and dominant carrier nonlinearity terms, demarcated by pump currents smaller and larger than the Fano factor

minimum/sharp loss regime, respectively.

3.4.4 A look towards phase noise

Thus far, I have just considered intensity noise. However, the well-known effect of amplitude-phase coupling in semiconductor lasers suggests interesting effects of nonlinear dispersive loss on phase noise and laser linewidth.

The phase noise can be calculated by noting $\delta\dot{\phi} = -\delta\omega = \frac{\alpha}{2}G_N\delta N + \beta\delta n$, so that

$$\omega^2\langle\delta\phi^\dagger\delta\phi\rangle = \frac{\alpha^2 G_N^2}{4}\langle\delta N^\dagger\delta N\rangle + \beta^2\langle\delta n^\dagger\delta n\rangle + \alpha G_N\beta\mathrm{Re}\left(\delta N^\dagger\delta n\right) \tag{3.8}$$

The effect of nonlinear dispersive loss on phase noise is the subject of further analysis.

3.5 Discussion

3.5.1 Experimental platforms

In this section, I describe some of the experimental platforms for realizing the effects described here. Because semiconductor platforms are conducive to integration with on-chip photonic crystal optical elements, many designs have already achieved the dispersive losses considered here and therefore could exhibit intensity noise reduction if quality factors and nonlinear strengths are within the tolerances required. For example, previous work has realized "Fano lasers" that exhibit self-pulsing due to the interplay between dispersive loss and carrier nonlinearity [42]. A Fano resonance is created by coupling between a waveguide and nanocavity (point defect) in a photonic crystal slab. By increasing the quality factor of the lasing waveguide mode in these types of structures, intensity noise reduction by nonlinear dispersive loss could be observable.

Photonic crystal surface-emitting lasers (PCSELs) are another platform that may be used for demonstrating the effects of nonlinear dispersive loss [46]. PCSELs may present advantages such as single-mode operation and high output powers; in contrast

to the Fano laser concept, lasing occurs transversely (and thus the Fano mirror is aligned transversely rather than longitudinally). However, because losses may be significant in both longitudinal and transverse directions, it is necessary to optimize quality factors in both directions. Nevertheless, advances in fabrication have achieved $Q > 5 \times 10^6$ in photonic crystal nanocavities, well within the background losses considered here [47].

In addition to Fano-type dispersive losses, distributed feedback-based losses have been commonly exploited to enforce single-mode operation. Examples include distributed Bragg reflector (DBR) fiber lasers, vertical cavity surface-emitting lasers (VCSELs), and DBR diode lasers [48, 49]. All of these architectures include sharply frequency dependent elements that may be used to achieve strong noise condensation. High quality fabrication is necessary to minimize background losses (e.g., scattering) at interfaces in order to observe the intensity noise condensation described here. In general, photonic crystals such as Fano mirrors and DBRs provide ideal platforms to realize sharply dispersive losses due to their geometrically-tunable photonic bandgaps. Combined with strong semiconductor optical nonlinearities, I foresee numerous experimental platforms that could exhibit the phenomena enabled by nonlinear dispersive loss.

Lastly, I note that even stronger nonlinearities are achievable in systems such as microdisk and quantum dot lasers due to enhanced confinement and ultralow mode volumes [50]. For mode volumes achieving λ^3, the dimensionless Kerr coefficient can be orders of magnitude larger than the values considered here. However, damage threshold intensities may also be lower, limiting the maximum shifts to refractive index and resonance frequency from Kerr nonlinearity. Nevertheless, these systems can exhibit ultrahigh quality factors, and are thus of potential interest for studying the effects presented here.

Lastly, combining the methodology described here with existing methods of pump noise reduction could yield even further intensity noise reduction.

3.5.2 Outlook

In this paper, I have shown how semiconductor lasers with sharply frequency dependent outcoupling and Kerr nonlinearity could be used to create lasers which produce high levels of intensity squeezing in the laser cavity. Additionally, I have demonstrated how strong carrier nonlinearities in these systems can lead to a new type of "carrier bistability" which leads to multiple possible laser steady states. I anticipate that many existing experimental platforms could realize the intensity noise condensation and bistable effects described here, especially systems employing a geometry that maximizes photonic (Kerr) nonlinearity over carrier nonlinearities, as in the external cavity-like geometry of Fig. 1 (with the gain being a semiconductor gain chip).

This work naturally suggests additionally possibilities for using nonlinear disperisve dissipation to control the output state of semiconductor lasers. Examples of topics for additional investigation include the effect of nonlinear dispersive loss on phase noise and linewidth, as well as the effects of optical feedback on intensity and phase noise (e.g., in external cavity lasers). Semiconductor lasers are ubiquitous in many real-world applications and I envision that the use of nonlinear dispersive loss could render them important sources of low noise states for use in sensing and quantum computing applications.

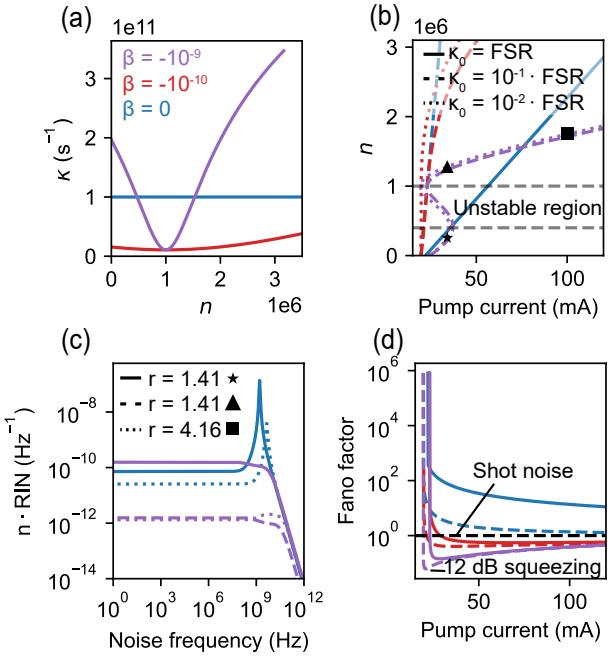

Figure 3-3: **Intensity noise squeezing in semiconductor lasers with dispersive photonic loss and intensity dependent nonlinearity.** (a) Intensity dependent loss profiles $\kappa(n)$ for three different (dimensionless) nonlinear strengths β ($\beta = 0$ corresponds to linear loss) coupled to symmetric Fano (Lorentzian) dissipation in the absence of carrier nonlinearity, as is a good approximation for an "external cavity" type geometry. (b) Steady state photon number n as a function of pump current (S-curve) for three different linear background losses κ_0 expressed as a fraction of the free spectral range FSR. The indicated unstable region is bypassed by the bistable point and is not generally accessible during lasing. (c) Fano factor spectrum ($n \cdot \text{RIN} \equiv \Delta n^2(\omega)/n$) as a function of noise frequency for three different pump powers $r \equiv I/I_{\text{thres}}$. Here, $\kappa_0 = \text{FSR}$ for the linear loss (blue) and $\kappa_0 = 10^{-2} \cdot \text{FSR}$ for the nonlinear loss (purple). (d) Fano factor as a function of pump current. Fano factors in (d) are plotted for the low noise (upper) branch in (b) when bistability is present. The Fano resonance decay rate is $\gamma = 2 \times 10^{12}$ rad/s.

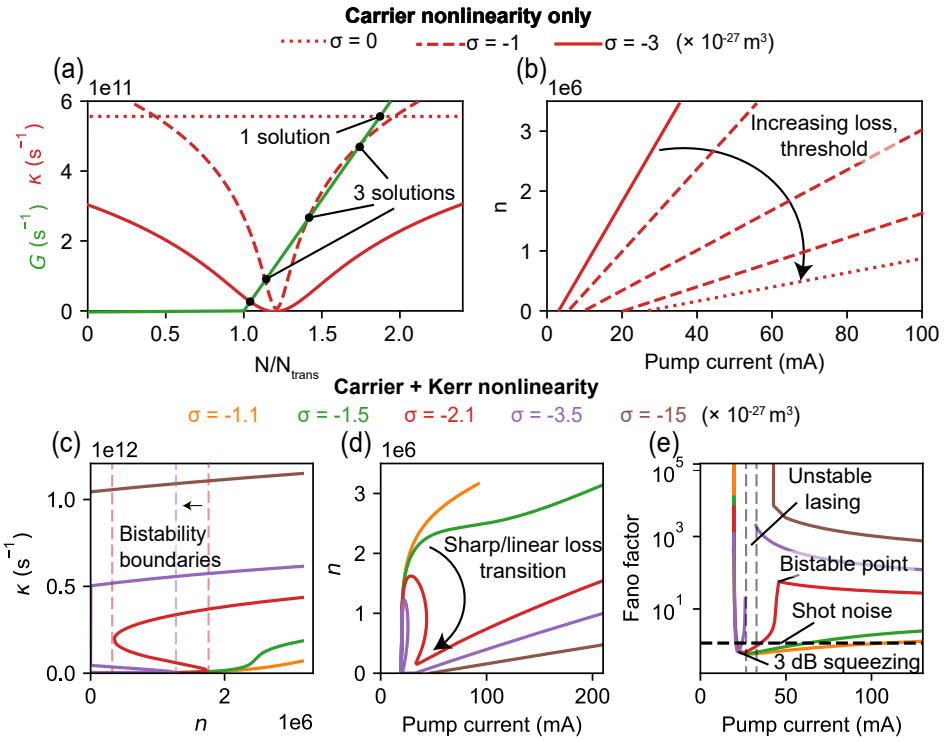

Figure 3-4: **Effects of carrier and Kerr nonlinearities composed with dispersive loss**. (a) Schematically, in the presence of only carrier nonlinearity σ, the resonance frequency and thus loss depend "directly" on carrier density N. Thus, "gain equals loss" implies $G(N) = \kappa(N)$ (both plotted as a function of the ratio of mean carrier density to transparency density). For sufficiently strong σ and low background loss κ_0, multiple steady state carrier densities N can correspond to a given photon number n, resulting in different losses (detunings from the Fano resonance). The lowest loss solution (smallest detuning) is most likely to lase, though extra solutions may be accessible by dynamic pumping schemes. (b) The schematic effect of this "carrier bistability" is to create multiple branches in the S-curve of different slope/threshold current. Interesting features emerge when both carrier and Kerr nonlinearities are present, resulting in the behaviors shown in panels (c), (d), and (e). In particular, the carrier nonlinearity causes a deformation of the intensity-nonlinear Lorentzian loss profile, eventually pinching off the "sharp loss" from the linear loss for sufficiently strong carrier nonlinearity (purple curve). This stems from leftward motion of the carrier bistability boundaries and creates a demarcation between linear ($F \gg 1$) and nonlinear ($F < 1$) loss regimes which may be separated by a region of lasing with no stable solution. System parameters used are the same as those in Fig. 3-3 with a nonlinear strength $\beta = -10^{-10}$, background loss $\kappa_0 = 10^{-2} \cdot \mathrm{FSR}$, and Fano resonance decay $\gamma = 2 \times 10^{12}$ rad/s. The magnitudes of Kerr and carrier nonlinearities taken here are comparable to what they might be in GaAs-based gain media: $\beta \sim -10^{-10}$ and $\sigma \sim -3 \times 10^{-27}$ m^3 (with the proviso of being taken as instantaneous and being evaluated at a single wavelength). Note also that the Kerr nonlinearity varies with mode volume (here, I consider a mode volume equal to the cavity volume).

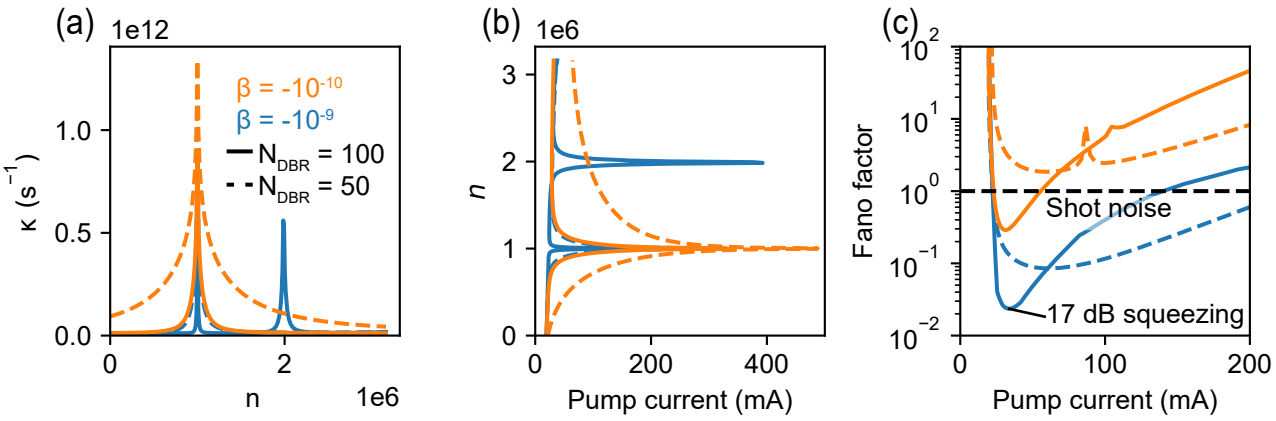

Figure 3-5: (a) Loss profiles for a DBR-based dispersive dissipation in the presence of Kerr nonlinearity. Here, the number of layer pairs N_{DBR} and strength of nonlinearity β are varied, with larger N_{DBR} and stronger β corresponding to sharper loss. In the most extreme case (solid blue curve), the loss is sharp enough to create two regions of sharp loss separated by a bistable region. (b) Corresponding S-curves, demonstrating how the sharp loss region $\kappa_n > 0$ occurs for forwards pumping (where a stop band switches to a pass band). (c) Integrated Fano factor plots, demonstrating strongly sub-Poissonian photon number noise, with maximum squeezing for sharpest loss (strongest nonlinearity and widest stop band). The artifacts near 100 mA are a result of amplitude-phase coupling. The effective refractive index and refractive index contrast are $\tilde{n} = 3.0, \Delta n = 1.23$ respectively. A linear background loss $\kappa_0 = 10^{-1} \cdot \mathrm{FSR}$ (quality factor $Q \approx 2 \times 10^5$) is assumed.

Chapter 4

Conclusions and Future Directions

In this thesis, I have described two projects related to state-of-the-art and next-generation sources of quantum states of light. My discussion thus far has focused on Fock states and intensity noise-squeezed states. However, since the writing of this thesis, I have begun investigating other methodologies for developing novel sources of other quantum states of light.

4.1 Generalizing nonlinear dispersive loss for quantum light generation

The phenomenon of nonlinear dispersive loss may be amenable to generating quantum states of light in systems other than those described here.

4.1.1 Intensity squeezing through electromagnetically induced transparency (EIT)

EIT, which arises from the destructive interference of two transition pathways in an atom, creates a transparency window in an otherwise opaque material. The typical setup is a three-level system coupled by pump and probe beams (the transparency window occurs in the latter). In addition to transparency, EIT is characterized by amplified nonlinear susceptibility; Kerr nonlinearities over 10 orders of magnitude

larger than those in conventional semiconductors have been observed in Rydberg atom Bose-Einstein condensate (BEC) systems exhibiting EIT, and recently this strength has been approached using Rydberg excitons in solid Cu_2O [51]. By placing such an EIT system in a high-Q cavity endowed with dispersive loss (as for example via photonic crystal elements), a loss that is sharply dependent on intracavity intensity can be created for the probe beam. This may induce unprecedented squeezing in intensity noise and represent the closest approach to a Fock state, limited only by background losses, which can be very low in the high finesse cavities common in atomic physics experiments. Thus, I expect EIT systems in high finesse cavities to be an ideal platform for the generation of highly number-squeezed radiation, eventually enabling the generation of high number Fock states.

4.1.2 Creating quantum states of light with second order nonlinearities and dispersive loss

Second order ($\chi^{(2)}$) nonlinearities, which are intrinsically stronger than Kerr nonlinearities, are often harnessed for parametric frequency conversion, mixing two waves and creating a third at the sum or difference of the two frequencies. Since these nonlinearities are intrinsically stronger than the Kerr nonlinearity discussed so far, these systems may come with new advantages for generating novel states of light in the presence of frequency dependent dissipation. Specifically, I propose studying an optical parametric oscillator (OPO), where a high-frequency pump is downconverted into two lower-frequency signal and idler beams, $\omega_p = \omega_s + \omega_i$. The frequency-dependent index of refraction depends on the electric fields as $n(\omega_{s,i}) \propto E_p E_{i,s}$ [52, 45]. The addition of sharply frequency dependent loss elements will create a system with complex coupled mode dynamics and amplitude-phase coupling absent in the Kerr nonlinear systems considered above. Depending on the details of the cavity and dispersive loss, different behaviors may emerge. For example, by varying geometric parameters of the setup, the resonances in the dispersive loss may be tuned such that each mode experiences lowest loss around some controllable photon number, with the nonlinear loss prevent-

ing fluctuations from this value. This could create a mixture or superposition of Fock states at degenerate or non degenerate frequencies. The amplitude-phase coupling induced by the $\chi^{(2)}$ nonlinearity may also enable phase noise squeezing, analogous to the use of external feedback and dispersive loss in semiconductor lasers. These systems are also amenable to on-chip applications with e.g. lithium niobate photonics, which could eventually lead to on-chip quantum light sources which are usable as resources for quantum information and more.

4.2 Other avenues

In addition to exploring the aforementioned two realizations of nonlinear dispersive loss, I am excited to explore other directions during my PhD, including:

1. Quantum multimode nonlinear optics (MMNLO). This is an area with considerable room for growth in both theory and experiment. For example, building on my machine learning background, I aim to develop a physics informed machine learning framework incorporating recent work on understanding multimode nonlinear interactions through the lens of thermodynamics as well as other physical constraints, potentially allowing a better physical picture of MMNLO [53]. By developing a quantum mechanical description of MMNLO, I also aim to explore how the integration of nonlinear dispersive loss in multimodal systems could realize highly entangled quantum states of unprecedented complexity.

2. Free electron interactions with nanophotonics have recently garnered significant interest for exhibiting quantum optical phenomena [54, 55, 56, 57, 58, 59]. One example is the recent demonstration of detecting heralded photons from free electron-photon entanglement [57]. I aim to study whether nanophotonics can be used to tailor free electron-photon interactions in such a way to deterministically create coherent and squeezed light of macroscopic intensities over an unprecedented wavelength range. This could, for example, result in the first demonstration of nanoscale free electron lasers, which could revolutionize laser

science and spectroscopy.

3. The study of strong and ultrastrong coupling (USC) is also one that is burgeoning. For example, strong coupling between solid state emitters and high-quality dielectric resonators have been applied for ultrasensitive magnetometry, while photonic quasiparticles formed from USC are thought to modify material properties [60, 61]. Can nanophotonics be used to amplify interactions between matter (such as solid state emitters) and photonic quasiparticles (such as polaritons) to create novel phases of quantum matter with photonic and matter-like character? This could be harnessed to boost the performance of classical photonic devices, from lasers to photovoltaics.

The generation of quantum light is a goal that will continue to guide the field of quantum optics, and I am excited by the potential contributions to this direction that my work may unlock.

Appendix A

Semiconductor Fock Laser Derivations

A.1 Derivation of $\langle 2D_{nn} \rangle$ correlator

In this section, we derive the photon number correlator in the presence of two-photon absorption (TPA). We begin with the equation of motion for photon number probabilities in the presence of TPA only, $\dot{p}_n = -\frac{\alpha_{\mathrm{TPA}}}{2} n(n-1)p_n + \frac{\alpha_{\mathrm{TPA}}}{2}(n+1)(n+2)p_{n+2}$, where p_n denotes the probability of having n photons inside the laser cavity. Thus,

$$\begin{aligned} \langle \dot{n} \rangle &= \sum_j j\dot{p}_j \\ &= -2\alpha_{\mathrm{TPA}} \sum_j j(j-1)p_j \\ &= -\alpha_{\mathrm{TPA}}[\langle n^2 \rangle - \langle n \rangle]. \end{aligned} \tag{A.1}$$

The RHS reduces to $-\alpha_{\mathrm{TPA}}\langle n \rangle^2$ assuming mean field theory, $\Delta n \ll \langle n \rangle$, recovering the equation of motion $\dot{n} = -\alpha_{\mathrm{TPA}} n^2$. Using the generalized Einstein relation, the correlator is $\langle 2D_{nn} \rangle = \frac{d}{dt}\langle n^2 \rangle - 2\langle nD_n \rangle$, where we express $\dot{n} = D_n + F_n$, with D_n a diffusion term and F_n a Langevin force. Thus

$$\begin{aligned}\langle 2D_{nn}\rangle &= \left(\sum n^2 \dot{p}_n\right) + 2\alpha_{\mathrm{TPA}}\langle n^3 - n^2\rangle \\ &= -\alpha_{\mathrm{TPA}}\langle n(n-1)^2\rangle + 2\alpha_{\mathrm{TPA}}\langle n^2(n-1)\rangle \\ &\approx 2\alpha_{\mathrm{TPA}}\langle n\rangle^2,\end{aligned} \tag{A.2}$$

again assuming mean field theory. Allowing for one-photon gain and loss, $\langle 2D_{nn}\rangle = 2\kappa n + \alpha_{\mathrm{TPA}} n^2 \to 3\kappa n$ for dominant TPA loss.

A.2 Linearized semiconductor rate equations and relative intensity noise

In this section, we provide a linearization of the semiconductor laser rate equations in the presence of various nonlinearities and calculate relative intensity noise using this formalism. We obtain

$$\begin{aligned}\delta\dot{n} &= -\left(\kappa_n n + \frac{pG_0}{2(1+p)}\right)\delta n + \left(G_N n - \kappa_N n\right)\delta N + F_n \\ &= -\left(\kappa_n n + \frac{pG_0}{2(1+p)}\right)\delta n + n\left(G_N - \kappa_N\right)\delta N + F_n \\ \delta\dot{N} &= -\left(\frac{G_0(1+p/2)}{1+p} - I_n\right)\delta n - \left(G_N n + \gamma_\parallel\right)\delta N + F_N.\end{aligned} \tag{A.3}$$

where $p = n/n_{\mathrm{sat}}$ denotes the saturation fraction for photon number and I_n denotes carrier generation by TPA. Note that G_0, G_N implicitly include the effects of gain saturation, $G_{0,N} \to G_{0,N}/\sqrt{1+p}$. Results in the main text assume $p, I_n \to 0$.

For simplicity of notation, we will introduce $a = nG_N + \gamma_\parallel, b = n\left(G_N - \kappa_N\right), c = G_0\frac{1+p/2}{1+p} - I_n, d = n(\kappa_n - G_n), \Gamma_1 = |a+d|, \Omega_R^2 = |ad+bc|$. Note that Ω_R^2 denotes the approximate relaxation oscillation frequency and Γ_1 the decay of relaxation oscillations. Fourier transforming the linearized rate equations,

$$\begin{bmatrix} -i\omega + d & -b \\ c & -i\omega + a \end{bmatrix} \begin{bmatrix} \delta n(\omega) \\ \delta N(\omega) \end{bmatrix} = \begin{bmatrix} F_n \\ F_N \end{bmatrix}, \tag{A.4}$$

yielding

$$\begin{bmatrix} \delta n(\omega) \\ \delta N(\omega) \end{bmatrix} = \frac{1}{-\omega^2 + (ad + bc) - i\omega(a + d)} \begin{bmatrix} (-i\omega + a)F_n + bF_N \\ -cF_n + (-i\omega + d)F_N. \end{bmatrix} \tag{A.5}$$

The intensity noise spectrum is then

$$\langle \delta n^\dagger(\omega)\delta n(\omega)\rangle = \frac{(\omega^2 + a^2)\langle 2D_{nn}\rangle + b^2\langle 2D_{NN}\rangle + ab\langle 2D_{Nn}\rangle}{(\omega^2 - \Omega_R^2)^2 + \omega^2\Gamma_1^2}. \tag{A.6}$$

As a side note, ignoring the effect of Kerr nonlinearity but including dispersive loss and the associated amplitude-phase coupling, we see that RIN can be reduced by a factor $(1+\kappa_\omega^2)/(1-\alpha_L\kappa_\omega/2)^2 \to 1/(1+\alpha_L^2)$ if the slope κ_ω is chosen appropriately, in agreement with earlier work on amplitude-phase decorrelation (where intensity noise is reduced somewhat at the expense of an increase in phase noise) [29]. However, this method leads to frequency selective squeezing, as opposed to the type of broadband squeezing we consider here.

We compute the Fano factor from Eq. 3.4 using the integrals

$$I_1 = \int_0^\infty \frac{1}{(\omega^2 - x^2)^2 + y^2} d\omega = \frac{\pi}{4y} \frac{\sqrt{2x^2 + 2\sqrt{x^4 + y^2}}}{\sqrt{x^4 + y^2}}$$
$$I_2 = \int_0^\infty \frac{\omega^2}{(\omega^2 - x^2)^2 + y^2} d\omega = \frac{\pi}{4} \frac{\sqrt{-2x^2 + 2\sqrt{x^4 + y^2}}}{\sqrt{x^4 + y^2}} + x^2 I_1,$$

where $x, y \in \mathbb{R}$. With $x^2 = \Omega_R^2 - \frac{\Gamma_1^2}{2}, y^2 = \Gamma_1^2\left(\Omega_R^2 - \frac{\Gamma_1^2}{4}\right)$, we have $I_1 = \frac{\pi}{2\Gamma_1\Omega_R^2}, I_2 = \frac{\pi}{2\Gamma_1}$. Thus, the Fano factor reads

$$F = \frac{1}{2n\Gamma_1\Omega_R^2}\left([\langle 2D_{nn}\rangle + n^2\kappa_{\dot{\phi}}^2\langle 2D_{\phi\phi}\rangle](\Omega_R^2 + a^2) + \langle 2D_{Nn}\rangle ab + \langle 2D_{NN}\rangle b^2\right) \tag{A.7}$$

A.3 Noise reduction from two photon absorption (TPA)

Two photon absorption (TPA), though not a dispersive loss, is weakly nonlinear in photon number and thus may be expected to permit some squeezing in intensity noise. When TPA is present, for large n,

$$F \to \frac{3\kappa}{2n(G_N + \alpha_{\mathrm{TPA}})}\left(1 + \frac{G_N}{\alpha_{\mathrm{TPA}} + \kappa/n}\right), \tag{A.8}$$

where $\alpha_{\mathrm{TPA}} = \kappa_n$. The minimum achievable Fano factor is $3/4$, obtained when $\kappa_0/n \ll \alpha_{\mathrm{TPA}} \ll G_N$ (here κ_0 denotes linear background loss). To obtain the TPA coefficient α_{TPA}, we use the relationship between intensity I and photon number $I \sim n\hbar\omega c/V$, so that $\alpha_{\mathrm{TPA}} \sim 2\hbar\omega c L\beta_{\mathrm{TPA}} \cdot \mathrm{FSR}/V$, where L, V respectively denote the length and volume of the cavity. For a cavity field oscillating at $\omega \sim 10^{15}$ Hz for GaAs at 1064 nm ($\beta_{\mathrm{TPA}} = 260$ m/TW), we find $\alpha_{\mathrm{TPA}} \sim 10^{-8} \cdot \mathrm{FSR}$ for $L \approx 1$ mm, $V \approx 10^{-16}$ m^3.

As shown in Fig. A-1a, TPA creates a sublinear S-curve that arises from the monotonic dependence of $\kappa(n)$ on n. Fig. A-1b demonstrates how TPA induces broadband intensity noise squeezing, resulting in a weak suppression of Fano factor (integrated over all noise frequencies) in Fig. A-1c. Linear loss asymptotes to unit Fano factor for large pump powers, while TPA can result in minor noise condensation (though this effect can be washed out if TPA is too strong or too weak, in violation of $\kappa_0/n \ll \alpha_{\mathrm{TPA}} \ll G_N$). The source of Fano factor reduction for higher pump currents is slightly different for both loss profiles. For linear loss, it occurs because steady state n increases linearly with pump current while the fluctuations $(\Delta n)^2$ have a sublinear dependence on pump current. In contrast, for TPA, the photon number n is clamped at high pump current and the photon number distribution is squeezed slightly due to the nonlinear loss $\kappa(n)$.

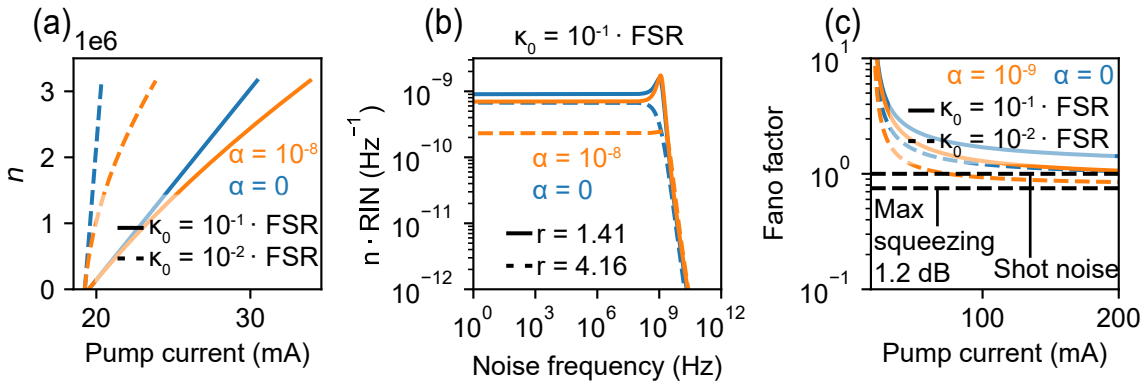

Figure A-1: (a) Steady state intracavity photon number as a function of pump current (S-curve), demonstrating sub-linear dependence of photon number with pump current for two-photon absorption (TPA). (b) Photon number variance spectrum for two different pump powers $r = I/I_{\text{thres}}$, with broadband squeezing for intensity dependent TPA. (c) Fano factor plots for linear and TPA loss profiles. The intensity dependence of TPA $\kappa(n) \propto n$ creates small (< 2 dB) drops in Fano factor below the shot noise limit when pumped far above threshold. Here, $\alpha \equiv \alpha_{\text{TPA}}/\text{FSR}$.

A.4 Steady states of Fano-based Fock laser

The oscillation condition requires that "gain equals loss" and that the cavity field is phase matched over a round trip through the resonator. The former condition was explicitly encoded in the rate equations and allowed us to determine steady state photon number. The latter condition reads

$$-\tan^{-1}\left(\frac{\delta}{\gamma}\right) + \frac{2\omega L}{c} n_{\text{eff}}(n, N) = 2m\pi, \tag{A.9}$$

where $n_{\text{eff}}(n, N) = n_{\text{eff},0}(1 + \sigma N + \beta n)$ is the shifted refractive index due to intensity and carrier nonlinearities and the amplitude reflectivity of the Fano mirror is $r_{\text{Fano}} = \frac{\gamma}{i\delta+\gamma}$ with γ the decay of the Fano resonance and $\delta = \omega - \omega_c$ the detuning from the Fano resonance centered at ω_c. We assume the second cavity mirror is broadband and imparts no phase shift (though a nonzero frequency independent phase shift can easily be incorporated without changing this analysis). If the phase shift of the Fano mirror was frequency independent, we would directly recover Equation 3.1 from the main text (ignoring constant phase offsets). The effect of the dispersive phase shift imparted by the Fano mirror is negligible over the detunings we consider: sweeping

across the Fano resonance gives a deviation from the prediction of Equation 3.1 of at most 0.02γ.

A.5 Carrier dependence of refractive index

The refractive index in the active region depends on carrier density as [42]

$$n_{\text{eff}}(\omega, N) = -\alpha G_N (N - N_{\text{trans}})/2\omega + n_b(\omega), \tag{A.10}$$

where we neglect the frequency dependence of the "bound" contribution to the refractive index $n_b \equiv n_b(\omega)$. Thus we can immediately associate

$$\sigma = -\frac{\alpha G_N}{2\omega n_b} \tag{A.11}$$

in Equation 3.1, explicitly showing the relationship between the carrier dependence of refractive index σ and the linewidth enhancement factor α. For example, GaAs/AlGaAs double-heterostructure lasers may have $G_N \approx 3 \times 10^4$ s^{-1} [62]. With linewidth enhancement factor $\alpha \approx 2$, $n_b \approx 3.5$ and $\omega \approx 10^{15}$ (telecom wavelengths), we find $\sigma \approx -10^{-27}$ m^3, consistent with the values used in the main text.

A.6 Active semiconductor Fock laser architecture

In this section, we introduce a special case of the semiconductor Fock laser architecture wherein the per-photon Kerr nonlinearity β comes from the gain medium itself, shown in Figure A-2. Importantly, since the medium is active, the Kerr nonlinearity is resonantly enhanced (typical values are provided in Table 3.1). For the purposes of our analysis, we will also assume that the index, and thus resonance frequency, responds instantaneously to changes in photon and carrier number relative to other timescales in the system, so that Specifically, here we ignore dispersive effects in the nonlinear strength near bandgap resonance. Materials and operating frequencies may need to be optimized so that this assumption is valid. For example, DBR lasers may

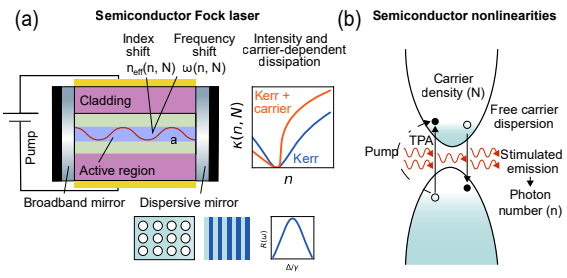

Figure A-2: **All-semiconductor Fock laser architecture.** (a) Basic semiconductor laser diode heterostructure design with nonlinear dispersive loss. Dispersive outcoupling is generated via the sharp frequency dependent transmission of a photonic crystal element. Coupling of combined Kerr and carrier nonlinearity with dispersive loss $R(\omega)$ creates sharp nonlinear loss $\kappa(n, N)$. Here, Δ denotes detuning from the dispersive (Lorentzian) resonance and γ denotes the width of the dispersive resonance (related to its FWHM). (b) Semiconductor optical nonlinearities, including intensity dependent Kerr effect as well as carrier-dependent free carrier dispersion (FCD) and two photon absorption (TPA). These nonlinearities shift the real part of the active region's refractive index, in turn shifting the resonance frequency in the diode cavity. Weak nonlinear loss from shifting the imaginary part of the refractive index via the Kramers-Kronig relations is also generated, but in most cases is negligible compared to the nonlinear dispersive loss.

be operated sufficiently far from the gain peak that the Kerr nonlinearity remains relatively large but can also be treated as instantaneous.

With this assumption of instantaneity of the Kerr nonlinearity, the results in Figs. 3-3 and 3-4 still hold, though larger nonlinearities may be accessible depending on the choice of material and cavity geometry.

Bibliography

[1] Toan Trong Tran, Christopher Elbadawi, Daniel Totonjian, Charlene J Lobo, Gabriele Grosso, Hyowon Moon, Dirk R Englund, Michael J Ford, Igor Aharonovich, and Milos Toth. Robust multicolor single photon emission from point defects in hexagonal boron nitride. *ACS nano*, 10(8):7331–7338, 2016.

[2] Mathijs de Jong, Luis Seijo, Andries Meijerink, and Freddy T Rabouw. Resolving the ambiguity in the relation between stokes shift and huang–rhys parameter. *Physical Chemistry Chemical Physics*, 17(26):16959–16969, 2015.

[3] Ramon Cuscó, Luis Artús, James H Edgar, Song Liu, Guillaume Cassabois, and Bernard Gil. Isotopic effects on phonon anharmonicity in layered van der waals crystals: Isotopically pure hexagonal boron nitride. *Physical Review B*, 97(15):155435, 2018.

[4] Ulrik L Andersen, Tobias Gehring, Christoph Marquardt, and Gerd Leuchs. 30 years of squeezed light generation. *Physica Scripta*, 91(5):053001, 2016.

[5] Daniel J Brod, Ernesto F Galvão, Andrea Crespi, Roberto Osellame, Nicolò Spagnolo, and Fabio Sciarrino. Photonic implementation of boson sampling: a review. *Advanced Photonics*, 1(3):034001–034001, 2019.

[6] Junaid Aasi, Joan Abadie, BP Abbott, Richard Abbott, TD Abbott, MR Abernathy, Carl Adams, Thomas Adams, Paolo Addesso, RX Adhikari, et al. Enhanced sensitivity of the ligo gravitational wave detector by using squeezed states of light. *Nature Photonics*, 7(8):613–619, 2013.

[7] Dirk Bouwmeester and Anton Zeilinger. *The physics of quantum information: basic concepts*. Springer, 2000.

[8] Thomas Jennewein, Christoph Simon, Gregor Weihs, Harald Weinfurter, and Anton Zeilinger. Quantum cryptography with entangled photons. *Physical review letters*, 84(20):4729, 2000.

[9] Nicholas Rivera and Ido Kaminer. Light–matter interactions with photonic quasiparticles. *Nature Reviews Physics*, 2(10):538–561, 2020.

[10] Matthew D Eisaman, Jingyun Fan, Alan Migdall, and Sergey V Polyakov. Invited review article: Single-photon sources and detectors. *Review of scientific instruments*, 82(7):071101, 2011.

[11] Axel Kuhn, Markus Hennrich, and Gerhard Rempe. Deterministic single-photon source for distributed quantum networking. *Physical review letters*, 89(6):067901, 2002.

[12] Stefania Castelletto and Alberto Boretti. Silicon carbide color centers for quantum applications. *Journal of Physics: Photonics*, 2(2):022001, 2020.

[13] I Aharonovich, S Castelletto, DA Simpson, CH Su, AD Greentree, and S Prawer. Diamond-based single-photon emitters. *Reports on progress in Physics*, 74(7):076501, 2011.

[14] Daniel Wigger, Robert Schmidt, Osvaldo Del Pozo-Zamudio, Johann A Preuß, Philipp Tonndorf, Robert Schneider, Paul Steeger, Johannes Kern, Yashar Khodaei, Jaroslaw Sperling, et al. Phonon-assisted emission and absorption of individual color centers in hexagonal boron nitride. *2D Materials*, 6(3):035006, 2019.

[15] J Hours, S Varoutsis, M Gallart, J Bloch, I Robert-Philip, A Cavanna, I Abram, F Laruelle, and JM Gérard. Single photon emission from individual gaas quantum dots. *Applied physics letters*, 82(14):2206–2208, 2003.

[16] Akbar Basha Dhu-al-jalali wal, Penchalaiah Palla, et al. Optical quantum technologies with hexagonal boron nitride single photon sources. *Scientific Reports*, 11(1):1–27, 2021.

[17] Emil V Denning, Jake Iles-Smith, Niels Gregersen, and Jesper Mork. Phonon effects in quantum dot single-photon sources. *Optical Materials Express*, 10(1):222–239, 2020.

[18] Claudio Parazzoli, Benjamin Koltenbah, David Gerwe, Paul Idell, Bryan Gard, Richard Birrittella, SM Rafsanjani, Mohammad Mirhosseini, OS Magan-Loiza, Jonathan Dowling, et al. Enhanced thermal object imaging by photon addition or subtraction. *arXiv preprint arXiv:1609.02780*, 2016.

[19] Hamidreza Akbari, Wei-Hsiang Lin, Benjamin Vest, Pankaj K Jha, and Harry A Atwater. Temperature-dependent spectral emission of hexagonal boron nitride quantum emitters on conductive and dielectric substrates. *Physical Review Applied*, 15(1):014036, 2021.

[20] Gordon Davies. Vibronic spectra in diamond. *Journal of Physics C: Solid state physics*, 7(20):3797, 1974.

[21] Gordon Davies. The jahn-teller effect and vibronic coupling at deep levels in diamond. *Reports on Progress in Physics*, 44(7):787, 1981.

[22] AA Maradudin. Theoretical and experimental aspects of the effects of point defects and disorder on the vibrations of crystals—1. In *Solid state physics*, volume 18, pages 273–420. Elsevier, 1966.

[23] Sahil Pontula, Jamison Sloan, Nicholas Rivera, and Marin Soljacic. Strong intensity noise condensation using nonlinear dispersive loss in semiconductor lasers. *arXiv preprint arXiv:2212.07300*, 2022.

[24] Benjamin J Lawrie, Paul D Lett, Alberto M Marino, and Raphael C Pooser. Quantum sensing with squeezed light. *Acs Photonics*, 6(6):1307–1318, 2019.

[25] Han-Sen Zhong, Hui Wang, Yu-Hao Deng, Ming-Cheng Chen, Li-Chao Peng, Yi-Han Luo, Jian Qin, Dian Wu, Xing Ding, Yi Hu, et al. Quantum computational advantage using photons. *Science*, 370(6523):1460–1463, 2020.

[26] Nicholas Rivera, Jamison Sloan, Yannick Salamin, and Marin Soljacic. Macroscopic condensation of photon noise in sharply nonlinear dissipative systems. *arXiv preprint arXiv:2111.03099*, 2021.

[27] S Machida, Y Yamamoto, and Y Itaya. Observation of amplitude squeezing in a constant-current–driven semiconductor laser. *Physical review letters*, 58(10):1000, 1987.

[28] Yoshihisa Yamamoto, Susumu Machida, and Wayne H Richardson. Photon number squeezed states in semiconductor lasers. *Science*, 255(5049):1219–1224, 1992.

[29] Michael A Newkirk and Kerry J Vahala. Amplitude-phase decorrelation: a method for reducing intensity noise in semiconductor lasers. *IEEE journal of quantum electronics*, 27(1):13–22, 1991.

[30] J Kitching, A Yariv, and Y Shevy. Room temperature generation of amplitude squeezed light from a semiconductor laser with weak optical feedback. *Physical review letters*, 74(17):3372, 1995.

[31] F Jérémie, C Chabran, and P Gallion. Room-temperature generation of amplitude-squeezed light from 1550-nm distributed-feedback semiconductor lasers. *JOSA B*, 16(3):460–464, 1999.

[32] Jesper Mork and Kresten Yvind. Squeezing of intensity noise in nanolasers and nanoleds with extreme dielectric confinement. *Optica*, 7(11):1641–1644, 2020.

[33] Takahiro Numai. Fundamentals of semiconductor lasers. *Fundamentals of Semiconductor Lasers*, pages 89–186, 2015.

[34] Mikkel Heuck, S Combrié, G Lehoucq, S Malaguti, G Bellanca, S Trillo, Philip Trøst Kristensen, Jesper Mørk, JP Reithmaier, and A De Rossi. Heterodyne pump probe measurements of nonlinear dynamics in an indium phosphide photonic crystal cavity. *Applied Physics Letters*, 103(18):181120, 2013.

[35] Yi Yu, Evarist Palushani, Mikkel Heuck, Nadezda Kuznetsova, Philip Trøst Kristensen, Sara Ek, Dragana Vukovic, Christophe Peucheret, Leif Katsuo Oxenløwe, Sylvain Combrié, et al. Switching characteristics of an inp photonic crystal nanocavity: Experiment and theory. *Optics express*, 21(25):31047–31061, 2013.

[36] Per Lunnemann, Sara Ek, Kresten Yvind, Rozenn Piron, and Jesper Mørk. Nonlinear carrier dynamics in a quantum dash optical amplifier. *New Journal of Physics*, 14(1):013042, 2012.

[37] AA Said, Mansoor Sheik-Bahae, David J Hagan, TH Wei, J Wang, James Young, and Eric W Van Stryland. Determination of bound-electronic and free-carrier nonlinearities in znse, gaas, cdte, and znte. *JOSA B*, 9(3):405–414, 1992.

[38] Govind P Agrawal. *Fiber-optic communication systems*. John Wiley & Sons, 2012.

[39] Govind P Agrawal. Effect of gain and index nonlinearities on single-mode dynamics in semiconductor lasers. *IEEE journal of quantum electronics*, 26(11):1901–1909, 1990.

[40] Demetrios N Christodoulides, Iam Choon Khoo, Gregory J Salamo, George I Stegeman, and Eric W Van Stryland. Nonlinear refraction and absorption: mechanisms and magnitudes. *Advances in Optics and Photonics*, 2(1):60–200, 2010.

[41] Weng W Chow, Stephan W Koch, and Murray III Sargent. *Semiconductor-laser physics*. Springer Science & Business Media, 2012.

[42] Yi Yu, Weiqi Xue, Elizaveta Semenova, Kresten Yvind, and Jesper Mork. Demonstration of a self-pulsing photonic crystal fano laser. *Nature Photonics*, 11(2):81–84, 2017.

[43] Luigi R Brovelli and Ursula Keller. Simple analytical expressions for the reflectivity and the penetration depth of a bragg mirror between arbitrary media. *Optics communications*, 116(4-6):343–350, 1995.

[44] HW Yen, W Ng, I Samid, and A Yariv. Gaas distributed bragg reflector lasers. *Optics Communications*, 17(3):213–218, 1976.

[45] Robert W Boyd. *Nonlinear optics*. Academic press, 2020.

[46] Susumu Noda, Kyoko Kitamura, Tsuyoshi Okino, Daiki Yasuda, and Yoshinori Tanaka. Photonic-crystal surface-emitting lasers: Review and introduction of modulated-photonic crystals. *IEEE Journal of Selected Topics in Quantum Electronics*, 23(6):1–7, 2017.

[47] Takashi Asano, Yoshiaki Ochi, Yasushi Takahashi, Katsuhiro Kishimoto, and Susumu Noda. Photonic crystal nanocavity with a q factor exceeding eleven million. *Optics express*, 25(3):1769–1777, 2017.

[48] John E Carroll, James Whiteaway, Dick Plumb, and RGS Plumb. *Distributed feedback semiconductor lasers*, volume 10. IET, 1998.

[49] Kenichi Iga. Forty years of vertical-cavity surface-emitting laser: Invention and innovation. *Japanese Journal of Applied Physics*, 57(8S2):08PA01, 2018.

[50] Kartik Srinivasan, Matthew Borselli, Oskar Painter, Andreas Stintz, and Sanjay Krishna. Cavity q, mode volume, and lasing threshold in small diameter algaas microdisks with embedded quantum dots. *Optics express*, 14(3):1094–1105, 2006.

[51] Michael Fleischhauer, Atac Imamoglu, and Jonathan P Marangos. Electromagnetically induced transparency: Optics in coherent media. *Reviews of modern physics*, 77(2):633, 2005.

[52] Ling-An Wu, Min Xiao, and HJ Kimble. Squeezed states of light from an optical parametric oscillator. *JOSA B*, 4(10):1465–1475, 1987.

[53] Fan O Wu, Absar U Hassan, and Demetrios N Christodoulides. Thermodynamic theory of highly multimoded nonlinear optical systems. *Nature Photonics*, 13(11):776–782, 2019.

[54] Aviv Karnieli, Nicholas Rivera, Ady Arie, and Ido Kaminer. The coherence of light is fundamentally tied to the quantum coherence of the emitting particle. *Science Advances*, 7(18):eabf8096, 2021.

[55] Roy Shiloh, Tomas Chlouba, and Peter Hommelhoff. Quantum-coherent light-electron interaction in a scanning electron microscope. *Physical Review Letters*, 128(23):235301, 2022.

[56] Ofer Kfir. Entanglements of electrons and cavity photons in the strong-coupling regime. *Physical review letters*, 123(10):103602, 2019.

[57] Armin Feist, Guanhao Huang, Germaine Arend, Yujia Yang, Jan-Wilke Henke, Arslan Sajid Raja, F Jasmin Kappert, Rui Ning Wang, Hugo Lourenço-Martins, Zheru Qiu, et al. Cavity-mediated electron-photon pairs. *Science*, 377(6607):777–780, 2022.

[58] Raphael Dahan, Alexey Gorlach, Urs Haeusler, Aviv Karnieli, Ori Eyal, Peyman Yousefi, Mordechai Segev, Ady Arie, Gadi Eisenstein, Peter Hommelhoff, et al. Imprinting the quantum statistics of photons on free electrons. *Science*, 373(6561):eabj7128, 2021.

[59] Valerio Di Giulio and F Javier García de Abajo. Free-electron shaping using quantum light. *Optica*, 7(12):1820–1830, 2020.

[60] Erik R Eisenach, John F Barry, Michael F O'Keeffe, Jennifer M Schloss, Matthew H Steinecker, Dirk R Englund, and Danielle A Braje. Cavity-enhanced microwave readout of a solid-state spin sensor. *Nature communications*, 12(1):1357, 2021.

[61] Anton Frisk Kockum, Adam Miranowicz, Simone De Liberato, Salvatore Savasta, and Franco Nori. Ultrastrong coupling between light and matter. *Nature Reviews Physics*, 1(1):19–40, 2019.

[62] T Takahashi, M Nishioka, and Y Arakawa. Differential gain of gaas/algaas quantum well and modulation-doped quantum well lasers. *Applied physics letters*, 58(1):4–6, 1991.